Summer 2007

Empirical investigation of enhanced air fins

Stephen John Dale Rucker

Recommended Citation

Rucker, Stephen John Dale, "Empirical investigation of enhanced air fins" (2007). *Masters Theses*. 4571.
https://scholarsmine.mst.edu/masters_theses/4571

EMPIRICAL INVESTIGATION OF ENHANCED AIR FINS

by

STEPHEN J. D. RUCKER

A THESIS

Presented to the Faculty of the Graduate School of the

UNIVERSITY OF MISSOURI–ROLLA

in Partial Fulfillment of the Requirements for the Degree

MASTER OF SCIENCE IN MECHANICAL ENGINEERING

2007

Approved by

K. O. Homan, Advisor

A. L. Crosbie

K. M. Isaac

ABSTRACT

Enhanced convective heat transfer surfaces have been a subject of interest for quite some time. Many different methods have been used to increase the amount of heat transfered from a surface. However, nearly all surface enhancement methods come with a price, frictional losses. This thesis studies the use of enhanced convective heat transfer surfaces on air fins in the laminar, transitional, and turbulent flow regimes with emphasis on the transitional regime. A major goal of this thesis is to further the understanding of the influence of an enhanced wall geometry on the transition from laminar to turbulent flow. Causing the flow to transition at a lower Reynolds number is typically a desirable effect because heat transfer from the surface is increased with a relatively small frictional loss increase.

The enhanced geometries studied are periodic bumped wall geometries with different ratios of the governing geometric parameters. Experimental tests to determine the heat transfer and friction characteristics of the surfaces over a range of Reynolds numbers from 600 to 3600 are discussed. Comparisons are made based on goodness factors that weigh the enhancement of heat transfer against the corresponding increase in frictional losses. Guidelines for selection of a bump geometry to promote high levels of heat transfer without causing large frictional losses are also presented.

ACKNOWLEDGMENTS

There are many people I owe thanks for their help during my research. I would like to thank Dr. Kelly Homan for being my advisor and guiding my research. Dr. Homan's knowledge and insight was very helpful throughout the entire process. I would also like to thank the distinguished members of my committee, Dr. Al Crosbie and Dr. Kakkattukuzhy Isaac. In addition, I owe thanks to Adams Thermals Systems, Inc. for sponsoring my research project.

I owe a great amount of thanks to my fellow lab workers Li-Kwen Chen, Jon Bridges, Kyle Benne, and Trent Taylor. Li-Kwen shared many interesting conversations with me relating to both research and his experiences. Kyle was a tremendous help in not only setting up the data acquisition system but also in debugging it. If something went wrong, I didn't even have to ask for Kyle's help because he was already there. Jon was an excellent resource when it came to setting up the experimental equipment. Since we were both simultaneously building flow loops, Jon and I were able to work together to solve all the problems that arose. Trent may not have been working on research related to heat exchangers, but his dedication to code debugging (FORTRAN or otherwise) was second to none and provided a source of inspiration.

I would also like to thank all the staff members of the Mechanical Engineering Department at UMR who have helped me over the past two years. In particular, I would like to thank Joe Boze, Randall Lewis, and Brian Mills for their help machining test sections. Without their expertise, none of the tests sections could have been produced.

Lastly, I want to thank my parents and family who have supported me throughout my research. It was always nice to know I had someone behind me throughout my work.

TABLE OF CONTENTS

LIST OF ILLUSTRATIONS

Figure Page

LIST OF TABLES

Table Page

NOMENCLATURE

Symbol	Description
A	area
B'_{mix}	modified second virial coefficient of mixture
C'_{mix}	modified third virial coefficient of mixture
C_D	discharge coefficient
C_f	Fanning friction factor
C_p	specific heat
$C_{f,m}$	length averaged Fanning friction factor
C	LVG chord length
D	duct inside diameter
D_h	hydraulic diameter
d	orifice bore diameter
d_w	screen wire diameter
d_{pt}	pressure tap hole diameter
E_{0,T_j}	voltage difference between ice bath and thermocouple bead
E_{std}	friction power per unit surface area
$E_{T_r,0}$	voltage difference between zone box and ice bath
E_{T_r,T_j}	voltage difference between zone box and thermocouple bead
$E_{T_r,T_{sum}}$	voltage difference between zone box and bulk temperature thermocouples
e	roughness element height
e^+	roughness Reynolds number, $\frac{e}{D_h}\sqrt{\frac{f}{2}}\mathrm{Re}$
e_s	saturated water vapor pressure
F_M	manometer correction factor
F_{EL}	elevation correction factor
$\overline{f}$	average friction factor

f	Fanning friction factor
f_e	enhancement factor
G	viscosity constant
H	channel height
H_2	bump half-height
H_g	height of LVG
H_s	smooth wall spacing
H_e^+	heat transfer correlation function
h	local heat transfer coefficient
h_m	length averaged heat transfer coefficient
h_w	orifice plate differential pressure
h_{da}	enthalpy per unit mass of dry air
h_{std}	heat transfer power per unit temperature difference per unit surface area
j	Colburn j factor, $\mathrm{StPr}^{2/3}$
j_m	length averaged Colburn j factor
K_L	loss coefficient
k	thermal conductivity
L	length
L_1	bump pitch
L_2	raised bump flat width
L_4	indented bump flat width
L_{pt}	pressure tap hole depth
Δl	LVG tip offset
l_w	screen wire spacing
M_a	molecular mass of air
Nu	Nusselt number, $\frac{hD_h}{k}$

Nu_m	length averaged Nusselt number
N_{vp}	units conversion factor
ΔP	pressure drop
Pr	Prandtl number, $\frac{c_p \mu}{k}$
P	pressure
p	roughness element spacing
$\dot{Q}_{cond}$	heat transfer rate due to conduction
$\dot{Q}_{conv}$	heat transfer rate due to convection
$\dot{q_h}''$	heat flux at heater
$\dot{q_w}''$	local wall heat flux
Re	Reynolds number, $\frac{\rho V D_h}{\mu}$
R	universal gas constant
R_e^+	roughness correlation function
St	Stanton number, $\frac{\mathrm{Nu}}{\mathrm{RePr}}$
St_m	length averaged Stanton number
T	temperature
T_b	bulk temperature
T_w	wall temperature
$\dot{V}$	volumetric flow rate
V	velocity
V_b	barometer output voltage
$\dot{W}_e$	electric heater power
W	channel width
W	humidity ratio
W_g	width of LVG
X	mole fraction
x^+	dimensionless position, $\frac{x}{D_h \mathrm{Re}}$

Y_1	gas expansion factor
Z	compressibility factor
α	angle of attack
β	chamfer angle
β_s	screen porosity
η_e	electric heater efficiency
ε_a	flow area goodness factor
γ	rib chamfer angle
μ	dynamic viscosity
ϕ	relative humidity
ρ	density
ρ_{f1}	density at upstream orifice pressure tap

1. INTRODUCTION

There is currently a need to develop more efficient heat transfer surfaces for use in off-highway equipment radiators. The heat transfer surfaces used in radiators can be compared using one of several metrics. One common measure of radiator efficiency relates the amount of heat rejected by the radiator to the given size and weight of the required equipment. The current drive is toward the use of radiators that are able to reject more heat than the current models while not adding a significant size, weight, or frictional loss penalty. This study investigated the enhancement of convective heat transfer for air fins currently in production by Adams Thermal Systems (ATS). The goal of this study was to increase the convective heat transfer from the fins while keeping the pressure drop due to friction to a minimum. Several different parameters were varied in an attempt to find an improved geometry for the air fins.

Typical operating conditions were given by ATS for the air fins. The working fluid was assumed to be dry air. The operating temperature range specified was 25°C to 70°C. The air velocity range through the fin channel was given as 3 to 15 m/s.

The fins currently in use by ATS were used as a baseline for comparison to new geometries. The baseline fins had bumps along the flow length to enhance heat transfer. An individual flow channel for the baseline fins had a roughly trapezoidal cross-section. The height was 9.525 mm, the base width was 2.04 mm, and the top width was 2.79 mm. The hydraulic diameter (D_h) for the baselines fin channel was found to be 3.85 mm. The flow length of the fins was 98.9 mm.

Reynolds number (Re) and Prandtl number (Pr) were found to aid in developing an experimental setup that preserved similitude between the actual fins and the experimental test channels. Reynolds number was found using Eq. (1).

$$\mathrm{Re} = \frac{\rho V D_h}{\mu} \tag{1}$$

Over the specified range of velocities and temperatures, the Reynolds number varied from 600 to 3600. Prandtl number was found according to its definition given in Eq. (2).

$$\mathrm{Pr} = \frac{c_p \mu}{k} \tag{2}$$

For the temperature range of 25°C to 70°, a constant value of 0.71 was found for Pr.

A single finned channel from a typical heat exchanger built by ATS was selected for experimental testing. The geometry was scaled to 10 times the production scale for testing purposes. Different bump geometries were machined into the side walls of the tested channels. Pressure drop measurements and temperature measurements were made along the length of the test section to determine the friction and heat transfer characteristics of the bumped surfaces.

In the thesis that follows, the first section is a review of literature. The review of literature gives a summary of past work in the area of heat transfer surface enhancement. Next, is a section discussing the design and implementation of the experimental program used to test the enhanced channels. A discussion of experimental results is the next section. In the discussion of results, the friction and heat transfer characteristics of the bumped walls are presented, compared to one another, and also compared to correlations from the literature. Finally, a summary of key results and recommendations for future work are given the last section.

2. REVIEW OF LITERATURE

2.1. CIRCULAR TUBES

The study by Nikuradse [1] was among the first to consider the effect of internal roughness elements on frictional pressure losses. Sand grain roughness was applied to the inside of tubes to evaluate the changes it caused. The effect of the sand grain roughness was studied over a wide range of Re from 600 to 10^6. One fundamental result of this study was that the effect of the roughness on the friction factor could be divided into three distinct Re ranges. In the range of low Re ($600 < \mathrm{Re} < 2160$), the values found for the friction factor were the same as those for a smooth tube without roughness elements. In the second range of Re ($2160 < \mathrm{Re} < 10^5$), the friction factor was found to depend on the relative roughness (e/D_H) and Re. The third range ($\mathrm{Re} > 10^5$) was determined by the range of Re where the friction factor became independent of Re and only depended on the relative roughness.

The explanation for these three ranges was given as follows. In the first range, the thickness of the boundary layer was larger than the average roughness element height. This resulted in losses due to friction which were approximately the same as those for a smooth pipe. In the second range of Re, the thickness of the boundary layer was about the same as the height of the average roughness element. Some elements were taller than the boundary layer and caused vortices to form and thus increased the friction factor. In the third range of Re, all the roughness elements were taller than the boundary layer thickness so a dependency on Re was no longer present.

Webb et al. [2] experimentally studied turbulent flow in a circular pipe with repeated rib roughness on the inside surface. The goal of the study was to find a general relationship between Stanton number (St) and friction factor for various configurations of ribs. The different rib geometries were described by using the rib height-to-pipe diameter ratio (e/D) and the rib spacing-to-rib height ratio (p/e).

The experimental findings were analyzed by considering boundary layer formation on the inside wall of the pipe. Webb et al. [2] found that the flow separated at the rib and then reattached to the wall at a certain distance downstream. Reattachment typically occurred at a distance downstream of the rib equal to 6-8 times p/e. At the reattachment point, a reverse flow boundary layer formed and grew in thickness in the upstream direction. Downstream from the reattachment point the boundary layer tended to redevelop until the next rib was encountered. It was found that the greatest value for the heat transfer coefficient (h) occurred at the reattachment point. It was also determined that the local heat transfer coefficient was larger in the separated flow region than in the regions where an undisturbed boundary layer was present.

2.2. RECTANGULAR CHANNELS

Han et al. [3] studied turbulent flow through rectangular channels with ribs. The study focused on the effect of changing rib shape, angle of attack (α), rib height-to-hydraulic diameter ratio (e/D_h), and the rib pitch-to-height ratio (p/e). The range of Re studied was $3000 < \text{Re} < 30,000$. Air was used as the working fluid in the experiments.

The experimental test channel in [3] used parallel plates that were 30.5 cm (12 in) wide and 152 cm (60 in) long. The distance between the plates varied from 1.3 to 2.5 cm (0.5 to 1 in). A total of 38 thermocouples were installed in the test section walls to measure local temperature. Heaters were placed on the walls to provide a constant heat flux boundary condition. To help minimize the uncertainty in the temperature measurements, the bulk temperature rise from inlet to outlet of the test section was between 22 and 33°C for all tests and the temperature difference between the test section wall and the fluid was between 17 and 22°C.

The first parameter studied was the rib height-to-hydraulic diameter ratio (e/D_h). For these tests the rib spacing-to-rib height ratio (p/e) was held constant at 5.0. It was found that for a given e/D_h the friction factor (f) approached a constant value as Re increased throughout the range studied. It was also found that St decreased as Re increased. Comparing different values of e/D found that as e/D increased St also increased. However, f also increased showing that more pumping power would be required for taller ribs. It was also found that it did not matter whether the ribs were directly opposite one another or staggered from one wall to the other.

The next parameter studied in [3] was the rib cross sectional shape. Modeling clay was used to fill in the corners of the originally square ribs. Filling in the corners of the ribs was found to be an effective way to decrease f while not significantly reducing St.

The effect of changing the rib pitch-to-rib height ratio (p/e) was studied for values of p/e= 5, 7.5, 10, 15, and 20. As p/e increased from 5 to 10, f and St were both found to increase. At $p/e = 10$ the maximum values for f and St were attained.

Varying the rib angle of attack (α) resulted in finding an optimal value for α that significantly reduced f while only slightly changing St. The four different angles of attack tested were $\alpha = 90°, 75°, 45°, \text{and } 20°$. The value of f was found to fall nearly 30% as α decreased from 90° to 45° while St only decreased 5%. At $\alpha = 20°$ the friction factor continued to decrease but St decreased sharply from the value at $\alpha = 45°$. So $\alpha = 45°$ was found to give the optimal combination of friction factor and Stanton number.

An experimentally determined correlation of the friction data was found for geometrically similar ribs. A geometrically similar family of ribs was created by keeping p/e, α, and the rib shape the same while varying e/D. The roughness function (R_e^+) was found to be related to the flow parameters as shown in Eq. (3).

$$R_e^+ = \frac{4.9\left(\frac{e^+}{35}\right)^m}{\left(\frac{\gamma}{90^\circ}\right)^{0.35}\left(\frac{10}{p/e}\right)^n\left(\frac{\alpha}{45}\right)^{0.57}} \tag{3}$$

where

$$m = \begin{cases} -0.4 & \text{if } e^+ < 35 \\ 0 & \text{if } e^+ \geq 35 \end{cases}$$

$$n = \begin{cases} 0.13 & \text{if } p/e < 10 \\ 0.53\left(\alpha/90^\circ\right)^{0.71} & \text{if } p/e \geq 10 \end{cases}$$

After finding R_e^+, the result was used in Eq. (4) to find the friction factor (f).

$$R_e^+ = \sqrt{\frac{2}{f}} + 2.5\ln\left(\frac{2e}{D}\right) + 3.75 \tag{4}$$

A correlation for St in terms of p/e, α, rib shape, and e/D was also found. This correlation was given in terms of a heat transfer function (H_e^+) as shown in Eq. (5).

$$H_e^+ = 10\frac{\left(e^+/35\right)^i}{\left(\alpha/45^\circ\right)^j} \tag{5}$$

where

$$i = \begin{cases} 0 & \text{when } e^+ < 35 \\ 0.28 & \text{when } e^+ \geq 35 \end{cases}$$

$$j = \begin{cases} 0.5 & \text{when } \alpha < 45^\circ \\ -.45 & \text{when } \alpha \geq 45^\circ \end{cases}$$

After finding H_e^+ and using R_e^+ found from the friction calculations, Eq. (6) was used to calculate St.

$$\text{St} = \frac{f}{\left(H_e^+ - R_e^+\right)\sqrt{2f} + 2} \tag{6}$$

In another study, Han [4] conducted experiments to examine the turbulent flow of air inside a square duct with ribs on two opposite walls. The range of Re tested was $7,000 < \text{Re} < 90,000$. The rib pitch-to-height ratio (p/e) was varied from 10 to 40 and the rib height-to-hydraulic diameter ratio (e/D_h) varied from 0.021 to 0.063. The test channel was 7.6 cm on each side and the ribs were placed on the two vertical sides. An unheated entrance section was used to ensure fully developed flow entering the test section. Woven heaters were placed on the channel walls to create a constant wall heat flux.

The first test consisted of varying e/D while holding $p/e = 10$ constant. It was found that the friction factor (f) approached a constant value as Re increased while St decreased with increasing Re. Increasing e/D caused both f and St to increase. The values for St were 1.8, 2.0, and 2.2 times the value for a smooth walled channel when $e/D = 0.021, 0.042,$ and 0.063, respectively. The value for St also increased 25% on the smooth walls due to the effect of the ribs on the flow.

Varying the value of p/e was the next test conducted in [4]. Values of 10, 20, and 40 were used for p/e while e/D was held constant at 0.063. Again, it was found that f approached a constant value as Re increased while St decreased with increasing Re. As p/e increased, it was found that both f and St decreased. For $p/e = 10$, St was 2.2 times the value for a smooth wall while for $p/e = 40$ the value for St was only 1.5 times the St value for a smooth wall.

Han [5] studied the effect of changing the aspect ratio of a rectangular channel with turbulent air flow. The channel had two ribbed walls and two smooth walls. The range of Re studied was $10,000 < \text{Re} < 60,000$. Five different channel width-to-channel height aspect ratios (W/H) were used with the ribs placed on the sides corresponding to W. The values tested for the aspect ratio were $W/H = 1/4, 1/2, 1, 2,$ and 4. The rib angle of attack was kept at 90° for all tests while the rib height-to-hydraulic diameter ratio (e/D_h) varied from 0.047 to 0.078. The rib spacing-to-rib height ratio (p/e) was tested for values of 10 and 20. A constant heat flux was applied to all the walls by a foil heater.

The effect of changing p/e was studied for both the smooth and the ribbed walls. For both values of p/e, the results for Nu were between 20-60% higher than Nu for a duct with four smooth walls. A periodic variation in Nu was established about three hydraulic diameters downstream from the entrance. Using $p/e = 10$ resulted in heat transfer coefficients between 10-20% higher than those found for $p/e = 20$.

Increasing the aspect ratio of the test channel caused Nu to increase. This increase in Nu was largely due to the fact that using a larger W/H caused the ribbed walls to be wider and the smooth walls to be narrower. A comparison was made between the different aspect ratios using the same surface area and pumping power. This comparison took into account the change in frictional losses due to the different aspect ratios. The performance parameter defined in Eq. (7) was used as the comparison metric.

$$\left(\frac{\mathrm{St}_r/\mathrm{St}(FD)}{\overline{f}/f(FD)}\right)^{1/3} \tag{7}$$

In Eq. (7) the subscript r designated the ribbed wall, St(FD) and f(FD) were values for a smooth walled channel with fully developed flow, and $\overline{f}$ was the average friction factor for the channel. For the ribbed wall, the performance parameter given in Eq. (7) decreased from 1.5 to 1.25 as W/H increased from 1/4 to 4. However, if a similar parameter was defined that used the average value of St for the channel (which included St on the the smooth and ribbed walls) in place of St_r, the parameter increased from 1.06 to 1.13 as W/H changed from 1/4 to 4 indicating better heat transfer performance per increase in pressure drop at $W/H = 4$.

Han et al. [6] experimentally tested the effect of changing the angle of attack of ribs in a short rectangular channel with turbulent air flow. A range of Re from 10,000 to 60,000 was used in the study. The different angles of attack (α) tested in the study were $90°, 60°, 45°,$ and $30°$. For these tests the ribs on the opposite walls were parallel from one side to the other. An additional test was performed for $\alpha = 60°$ with the ribs on opposite wall in a crossed configuration. Aspect ratios (W/H) of 1/2 and 1/4 were used in the tests. The length of the channel was varied from 10 hydraulic diameters to 15 hydraulic diameters. The rib height-to-diameter ratio (e/D_h) was set to 0.047 and 0.078. The rib spacing-to-rib height ratio (p/e) was tested at 10 and 7.5. The test channels had a constant heat flux provided by foil heaters attached to all the walls.

The study found that α had a large influence over Nu in channels with narrow aspect ratios. A ratio of Nusselt numbers was used to compare the channel with ribbed walls to a channel with all smooth walls and fully developed flow (FD). This ratio was given as shown in Eq. (8).

$$\frac{\mathrm{Nu}}{\mathrm{Nu}(FD)} \tag{8}$$

The Nu ratio was found to increase for $\alpha = 60°$ and $\alpha = 45°$ when compared to the value found with $\alpha = 90°$. For $\alpha = 30°$ the Nu ratio was close to the same as for $\alpha = 90°$. Comparing the results for a channel with crossed ribs to the results for a channel with parallel ribs found that the crossed ribs yielded nearly the same Nu ratio as the parallel ribs. The Nu values for the crossed ribs were slightly lower at locations farther downstream in the channel, but the differences were not significant.

The enhancement of heat transfer found by using the ribs in the configurations discussed was accompanied by an increase in pressure drop through all the channels when compared to a smooth channel. A comparison was made of the different channel configurations using the parameter given in Eq. (7). This comparison assumed constant pumping power was used throughout all the channels. For a narrow aspect ratio channel the highest value for thecomparison parameter was attained when $\alpha = 45°$.

2.3. RESONANT HEAT TRANSFER

Greiner et al. [7] introduced the idea of resonant heat transfer where an intermittent wall geometry was used that consisted of an enhanced surface followed by an unenhanced surface. The idea behind resonant heat transfer is that the enhanced surface excites waves in the flow that persist into the unenhanced region of the channel. The particular geometry studied in [7] was a flat walled recovery section downstream of grooved wall section. The range of Re studied was from 1500 to 5000. The test section had a minimum wall-to-wall spacing of 10 mm in the grooved portion and a height in the flat-walled portion that was also 10 mm. The width of the test section was 203 mm throughout and the length was 1.10 m. In the grooved portion, the grooves were only cut in the bottom wall and had a base width of 24 mm and a depth of 12 mm. Surface temperature measurements were made using 18 thermocouples and pressure drop measurements were made at 24 different points through 2 mm diameter pressure tap holes.

The key result from [7] was that in the flat walled recovery region the friction factor went back to its flat channel value much quicker than the heat transfer coefficient. As Re increased, the flow length required for both the friction factor and heat transfer coefficient to decay to their flat walled values decreased, but the friction factor still always decayed faster. These results show that over short recovery lengths the heat transfer would only be slightly less than if the grooved region had continued, but the friction factor would be significantly reduced. For a recovery length equal to 5.4 hydraulic diameters ($L/D_h = 5.4$), it was found that pumping power could be reduced 44% and the same Nu would be maintained. A longer recovery length of $L/D_h = 11.6$ was found to allow a 30% decrease in pumping power to maintain the same Nu.

Greiner et al. [8] numerically studied another intermittently grooved channel. The channel had the same cross-sectional and groove dimensions as the one studied in [7] but in the grooved portion both the top and bottom walls were symmetrically grooved. In addition, the overall length of the channel was only 0.336 m (14 groove lengths) with the first half grooved and the second half smooth. The range of Reynolds numbers used was from 600 to 1800.

The major finding from [8] was that Nusselt number remained enhanced for up to six groove lengths into the flat walled portion of the channel. The maximum enhancement length of six groove lengths was found for Re = 1800 while for Re = 600 the enhancement length was only three groove lengths. The friction factor dropped back to its corresponding flat walled value in only three groove lengths for all Re. Based on these findings only a small gain in heat transfer for a given pumping power could be realized for Re = 600. However, for Re = 1200 and Re = 1800 a significant gain was found. The explanation given for the different amounts of enhancement was that at Re = 600 the flow was essentially steady with no travelling waves. Once Re reached 1200, travelling waves were present that travelled several groove lengths into the flat walled region enhancing heat transfer more so than friction factor.

2.4. LONGITUDINAL VORTEX GENERATORS

An interesting geometry that was considered for enhancing air-side fins was longitudinal vortex generators (LVG). The idea behind the use of LVG's is to use a surface protuberance to generate vortices in the streamwise direction as described in [9]. Jacobi and Shah [9] described how LVG's are usually used in pairs to generate a set of counterrotating vortices similar to the horseshoe vortices present when air flows around a finned tube. The vortices thin the boundary layer on the fin and thus enhance heat transfer from the fin. However, the LVG's also incur a pressure drop penalty due to their disruption of the flow.

One key parameter that determined how effectively the LVG's performed was the height of the protuberance. In [9] it was reported that the LVG needed to have a height at least as high as the local boundary layer thickness. Garimella and Eibeck [10] used a single row of rectangular LVG's and tested two different heights of LVG's. One set of LVG's was twice the height of the other set. The taller LVG's had a peak heat transfer enhancement of 41% while the shorter LVG's had a peak enhancement of 30%. Pressure drop information was only given for the taller LVG's where the average pressure drop increase was 7% across the range of Reynolds numbers studied. Another interesting result from [10] was that the LVG's seemed to be better suited for use in the laminar and transititional flow regimes. Garimella and Eibeck [11] found that the optimal ratio of the LVG height to channel height decreased with increasing Reynolds number.

The angle of attack of the LVG's was another important parameter. Tiggelbeck et al. [12] studied two winglet LVG geometries over a range of Reynolds number from 2000 to 9000. The angle of attack was varied between 30° and 90° during testing.

The results of varying the angle of attack showed that the maximum heat transfer enhancement occurred for an angle of roughly 60°. At a 60° angle of attack the Nusselt number was enhanced about 1.8 times over the Nusselt number for a plain fin. The drag coefficient also increased above the value for a plain fin by 3.2 times. From [12] it was also noted that for an angle of attack of only 30° the Nusselt number was enhanced to 1.5 times the plain fin value and the drag coefficient was 1.9 times the value for a plain fin. This finding emphasized the fact that the drag coefficient increased at a faster rate than the Nusselt number as the angle of attack increased.

Most of the LVG geometries studied were produced by punching through a sheet of fin material to create the raised geometry. However, this method would not be desirable for an air fin subjected to air containing a large proportion of particulate matter, such as in off-highway applications. A study was found in [13] that used embossed LVG's that would not require holes to be placed in the fin material. In [13] semi-cylindrical LVG's were embossed on a plain fin. The range of Reynolds numbers studied was from 1000 to 5000. The LVG's were periodically arranged in pairs with an angle of attack equal to 45°. The LVG's were 72 mm across their base and 10 mm high. The overall flow channel had a rectangular cross-section with a height of 860 mm and a width of 27 mm. The LVG's were mounted on the side walls of the test section. The results of the study showed that the semicylindrical LVG's were very effective at generating vortices that thinned the boundary layer which should result in heat transfer enhancement. The intensity of the vortices increased as Reynolds number increased. A very interesting result was that the intensity of the vortices always reached its maximum level after the flow passed over only three rows of LVG's. For Reynolds numbers above 2000, the vortex intensity had already saturated after only one row of LVG's.

2.5. USE OF FINDINGS

The findings from this literature review were used to aid in the development of the experimental testing program. It was noted that nearly all work for rib enhanced walls had been done in the turbulent flow regime. However, the current study was geared toward a range of Re that would fall under the laminar or transitional flow regime. Tests studying the effects of varying geometric parameters for the current bumped fins were performed in a similar fashion to the tests performed in [3], [4], [5], and [6]. The work performed in [7] and [8] provided guidance for tests using an intermittent enhanced wall geometry. It was desired to find if the same significant advantages noted in those studies could be realized using the current ATS bumped fin geometry or another enhanced geometry. The use of the information from the LVG studies is discussed later in the test section design section.

3. EXPERIMENTAL DESIGN AND PROCEDURES

3.1. EXPERIMENTAL SETUP

An air flow loop was constructed for use in the experimental tests. The flow loop used for the experimental testing of air fins is shown in Figure 3.1. A detailed description of the key components is given in the following sections.

3.1.1. Ducting. The ducting used for the majority of the loop was clamp-together sheet metal ducting from K&B Duct. The clamp-together style of duct was selected due to the adjustability and ease of installation. The use of adjustable couplers on the ducting made it very easy to adjust the length of specific portions of the ducting. This adjustablity was particularly useful when accommodating various test section lengths. There were, however, issues of getting a good air tight seal when using the clamp-together ducting. To help ensure a good seal, Nashua 765 Duct

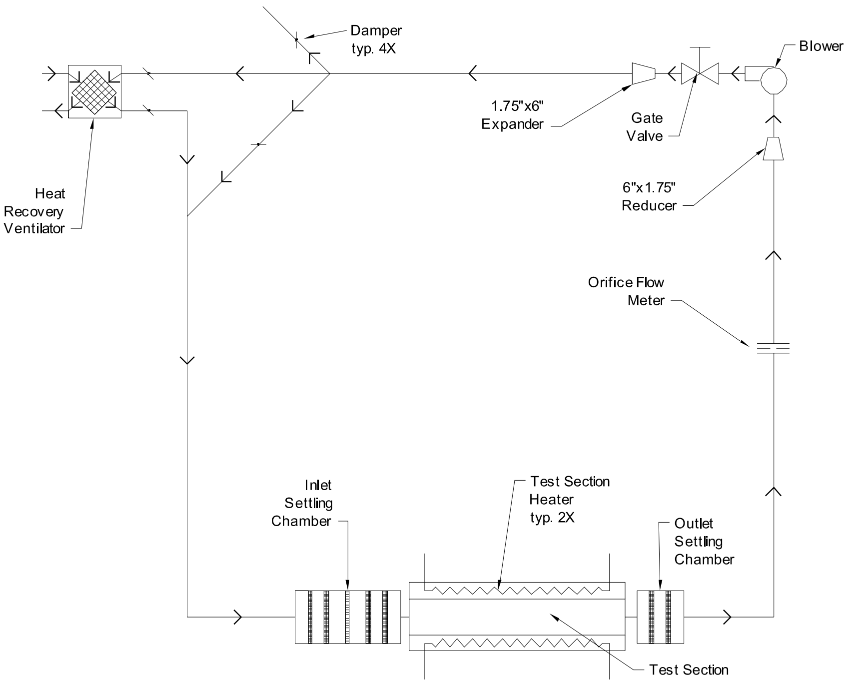

Figure 3.1: Flow loop component diagram

Sealant Mastic and GB Duct Seal were used to fill and seal all joints and seams in the ducting. The only portion of ducting that had to be perfectly air tight was from the outlet settling chamber to the orifice flow meter. In this area PVC ducting was substituted for the metal ducting. All joints were both PVC cemented and sealed with duct mastic to ensure no leakage. A test was performed to verify that no air leakage occurred and is described in Section 3.7.1.

Calculations of pressure drop through the flow loop over the anticipated range of flow rates were made to aid in the selection of the ducting. The calculations showed that the pressure drop would not exceed 1744 Pa (7 in w.g.) when 15.24 cm (6 in) inside diameter ducting was used. Smaller inside diameter ducting was considered but resulted in pressure drops that were too large for any available blowers at the required flow rates. Based on these findings, the selected size of ducting was 15.24 cm (6 in) inside diameter ducting. This size also helped keep the air velocity below 2.54 m/s as suggested in [14]. Having low air velocity in the ducting kept the noise to an acceptable level during operation. All the ducting was insulated with a layer of R-13 fiber glass insulation which not only helped thermally insulate the duct but also further reduced the noise.

3.1.2. Blower. The blower used in the air flow loop was Ametek model number 116637M with a variable speed control. This model of blower had a maximum volumetric flow rate of 0.0472 m^3/s (100 cfm) and could overcome up to 6750 Pa (27.1 in w.g.) static pressure loss. This blower was one of few available that could operate at the low flow rates and high static pressures required in the flow loop without having problems caused by fan surge. A useful feature of the selected Ametek blower was its variable speed motor. The variable speed motor allowed the blower to operate over a wide range of flow rates and static pressures thereby eliminating the need for different blowers for different test cases.

3.1.3. Heat Recovery Ventilator. A heat recovery ventilator (HRV) from Nu-Air Ventilation Systems was used to preheat the incoming room air that was used in the loop. A model NU120-2 with aluminum core HRV was used. The HRV used warm exhaust air to heat the incoming air in a cross flow heat exchanger core. The fact that the HRV was not 100% effective at warming the incoming air was a desirable feature. The amount of heat lost in the HRV due to inefficiency helped offset the amount of heat added in the test section so steady-state operation of the loop could be attained.

3.1.4. Orifice Flow Meter. A thorough study of possible flow meters for the flow loop was performed. Upon completion, it was found that a quadrant-edged orifice plate flow meter was best suited in terms of range of performance and cost. The quadrant or quarter-circle edge of the orifice bore allowed this type of orifice plate to be used at much lower Reynolds number than a typical square-edged orifice plate. The quadrant-edged orifice plate offers the advantage of a constant discharge coefficient over a wide range of Reynolds numbers. The range of flow rates required for the tests performed in the flow loop was from $7.08\text{x}10^{-4}$ to $3.07\text{x}10^{-2}$ m^3/s (1.5 to 65 cfm). To cover this range and have an acceptable level of accuracy in the measurements, two different orifice plates were required. One plate was sized for flows from $4.72\text{x}10^{-4}$ to $1.37\text{x}10^{-2}$ m^3/s (1 to 29.5 cfm) with a corresponding differential pressure range of 0.572 to 498.2 Pa (0.0023 to 2 in w.g.). The second plate was sized for flow rates from $5.67\text{x}10^{-3}$ to 0.03069 m^3/s (12 to 65 cfm) with the highest differential pressure again being 498.2 Pa (2 in w.g.). When sizing the orifice bore, the maximum differential pressure across the orifice plate was selected based on the range of the Dwyer Microtector manometer used to make pressure measurements. The orifice plates used to measure flow rate were purchased from Lambda Square, Inc. When installed in the flow loop, the orifice plate was bolted between two 150# ANSI flanges after being sandwiched between PVC orifice holding blocks and Buna-N gaskets as shown in Figure 3.2. By observing the guidelines and recommendations given by Miller [15], the expected uncertainty in the discharge coefficient for the orifice flow meter was ±2.5%.

3.1.5. Band Heater. A band heater was purchased and installed on the ducting to help heat the inlet temperature to the desired level. The selected heater was an Omega MBH-60201000T that had a maximum heat output rate of 1000W. To help control the amount of heat being added by the band heater a Superior Electric 116C variac transformer was used to control the input voltage and thus the power output through the heater.

3.1.6. Flow Conditioning. Flow conditioning at both the inlet and outlet of the test section was accomplished using settling chambers with screens and honeycomb straighteners. The inlet settling chamber is shown schematically in Figure 3.3. As shown in the figure, there were four insect screens with a mesh count of 7.09x6.30 wires per cm (18x16 wires per in) and one section of honeycomb used to condition the flow. The wire diameter of the screens was 0.28 mm (0.011 in) and the material was aluminum. The screens were selected based on the suggestions in [16] that the overall loss coefficient of the combination of screens be 2.8 to reduce the turbulent intensity and promote a uniform velocity profile. Each screen had a loss coefficient of roughly 0.7 found by using Eq. (9) as given in [16].

$$K_L = 0.52\left(1 - \beta_s^2\right)/\beta_s^2 \tag{9}$$

In Eq. (9) K_L is the loss coefficient and β_s is the porosity of the selected screen,

$$\beta_s = \left(1 - d_w/l_w\right)^2 \tag{10}$$

found to be 0.661. In Eq. (10) d_w is the screen wire diameter and l_w is the spacing between wires.

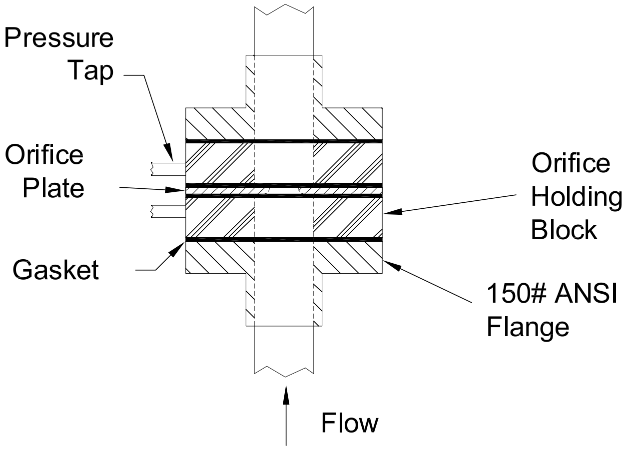

Figure 3.2: Orifice installation diagram

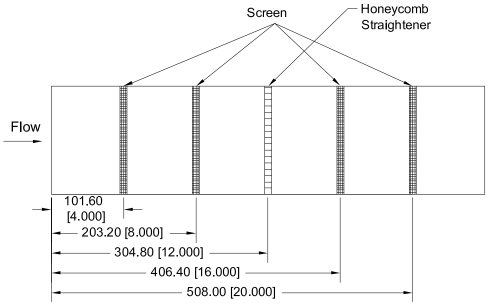

Figure 3.3: Inlet settling chamber

The honeycomb was selected based on information found in [17]. The flow length-to-hydraulic diameter ratio was approximately eight for the selected honeycomb which fell in the range suggested by [17]. The loss coefficient for the honeycomb was found to be 0.5 from information in [17].

The spacing between the components of the inlet settling chamber was determined based on information in [17]. One suggested screen separation distance was to set the separation equal to at least 500 screen wire diameters. A second suggested separation distance was 30 times the screen opening. After performing calculations to find both of these values, it was found that a spacing of 10.16 cm (4 in) between components would be a compromise between the suggested spacings. The cross-section of the inlet settling chamber was a rectangle 3.15 cm (8 in) wide by 2.36 cm (6 in) high. The cross-sectional size was selected to give a flow area reduction slightly above the range of 7 to 12 as suggested in [17] for the two sizes of test sections used. The inlet settling chamber was constructed from Plexiglas.

The outlet settling chamber was similar to the inlet settling chamber but it only used two insect screens to condition the flow. The screens were the same as those used for the inlet and they were again spaced 10.16 cm (4 in) apart. The cross-section of the outlet settling chamber was 3.94 cm wide by 2.36 cm tall (10 in wide by 6 in tall) and the outlet settling chamber was also constructed from Plexiglas.

3.1.7. Inlet and Exit Conditions. Since the air fins that were tested in the flow loop came from a radiator, the inlet and exit conditions that were felt to be most appropriate were a sudden contraction inlet and a sudden expansion outlet. These conditions best match what would be found for the air fins in actual operation. To accomplish both of these conditions the test section was attached to a phenolic flange plate on each end with a sharp edged transition from the settling chamber to the test section.

3.1.8. Bleed Off Cap. If the flow loop was operated with the test section inlet temperature close to room temperature then the amount of heat lost at the HRV was not enough to balance the heat input at the test section. This would make steady state impossible to attain for these temperatures. To avoid this problem, the flow loop was designed with a bleed off cap that would vent the exhaust air to the room rather than having it pass through the HRV. Having the exhaust air bypass the HRV prevented the intake air from being warmed and allowed steady state operation at inlet temperatures close to room temperature. A damper was installed just before the bleed off port to help control how much of the exhaust air was bled off.

3.2. TEST SECTION DESIGN

Two different scales of test sections were experimentally tested. The first scale was the same scale as currently used in production by Adams Thermal Systems. The second scale was 10 times the current production scale. Use of the larger scale meant that the instrumentation could be placed with much more precision and will allow for future instrumentation, such as for hot wire anemometry. All test sections were machined from 6061-T6 aluminum.

3.2.1. Production Scale Test Sections. Two different test sections were tested on the production scale. Both were smooth walled channels that were used to verify the accuracy of the setup and measurement systems.

The first production scale test section was a smooth walled channel made from Plexiglas designated afn000. The flow channel had a rectangular cross-section with dimensions of 9.525 mm (0.375 in) high by 203.2 mm (8 in) wide and was 546 mm (21.5 in) long. Test section afn000 was only used for pressure testing to determine the friction characteristics. The length of afn000 was not taken directly from the current production fins but instead was made longer to determine the flow length required for hydrodynamically fully developed flow. Static pressure taps, with geometry as discussed in Section 3.2.6, were drilled along the centerline of the channel. In all, 18 pressure taps were used to measure the pressure drop along the flow length. The pressure taps were clustered at the inlet and outlet to capture any changes due to the entrance or exit from the test section. Between the inlet and outlet pressure tap clusters the pressure taps were evenly spaced along the length.

Test section afn001 was the second production scale test section. Test section afn001 was machined from 6061-T6 aluminum and had the same cross-sectional dimensions as afn000 but had a shorter length of 111.6 mm (4.393 in) which was only 12.7 mm (0.500 in) longer than the current production fins. The extra length compared to the production fins was required to mount the test section in the phenolic flange plates. Test section afn001 was used for temperature measurements to find the heat transfer characteristics of the channel. The channel was heated using the mica heaters described in Section 3.2.8 mounted on the top and bottom walls. Temperature measurements were made using thermocouples installed in 18 thermocouple holes drilled in the top wall and six thermocouples holes in the bottom wall. The thermocouple holes were drilled as described in Section 3.2.7. Thermocouples were installed in both the top and bottom walls to check if natural convection was playing a significant role in the heat transfer through the walls.

3.2.2. Scaled Test Sections. Seven different test sections were tested that were scaled at 10 times the production scale. All the scaled test sections had smooth walls for the top and bottom of the channel and all but one of the test sections had an enhanced surface on the side walls. Due to the length of the test sections exceeding the maximum travel of the CNC mill used for the machining operations, the overall channel was machined in several portions that were assembled to make the test section. The top and bottom walls were split into three portions and each of the side walls was split into two portions.

The top and bottom walls of all the scaled up channels were the same. The top had three pressure tap holes and eight thermocouple holes along its centerline. The bottom had eight thermocouple holes though not all the thermocouples were used during all the tests due to a limited number of available data acquisition channels. An additional two thermocouples were placed in the top and bottom 152.4 mm (6 in) from the inlet offset from the centerline to measure the temperature directly above the corner where the top or bottom met the side. These thermocouples were used in conjunction with thermocouples mounted near the corner in the sides to verify that the top and bottom of the channel were at the same temperature as the sides. The same setup of offset thermocouples was placed 152.4 mm (6 in) from the test section outlet. Thermocouples were only installed in one of the sides of the scaled up test sections. The side with the thermocouples was referred to as side A and the side with no thermocouples along the centerline was referred to as side B.

Only three pressure taps were used in the scaled up test sections because the pressure drop across the entire test section was predicted to never exceed 24.91 Pa (0.100 in w.g.). As a result, the use of more than three pressure taps would have resulted in pressure drops with large uncertainties even when measured with the Microtector manometer.

For the scaled up test sections similitude was maintained between the production scale fins and the scaled up fins. Geometric similitude was maintained by scaling all production dimensions by a factor of 10. Dynamic similitude was realized by using the same Reynolds numbers between the two scales and using the same working fluid of air which meant the Prandtl number was the same.

3.2.3. Smooth Walled Test Sections. One scaled up test section was tested where the side walls were smooth. This test section was designated sfc000. Test section sfc000 had a rectangular cross-section with a height of 95.25 mm (3.750 in), a width of 25.40 mm (1.000 in), and was 1202.6 mm (47.347 in) long. Both pressure and temperature tests were performed using sfc000. Three pressure tap holes were drilled in the top of the test section. There were 29 thermocouples installed along the centerline of side A for temperature measurements. The thermocouples were closer together at the inlet and exit to capture any entrance or exit effects.

3.2.4. Bumped Wall Test Sections. Four different test sections were tested that had a bumped wall geometry on the side walls of the test section. The basic cross-section of all these test sections was rectangular with a height of 95.25 mm (3.750 in), a width of 25.40 mm (1.000 in), and were 1202.6 mm (47.347 in) long. The notation used to describe the bumped wall geometry is shown in Figure 3.4. An image of a representative bumped wall is shown in Figure 3.5. The values for all the

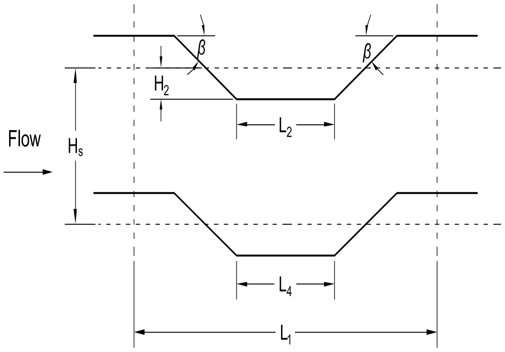

Figure 3.4: Notation for bumped wall geometry

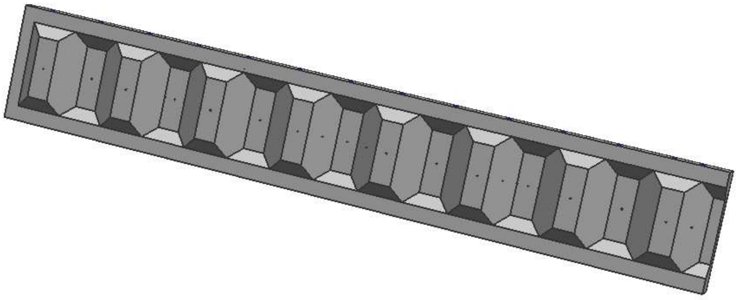

Figure 3.5: Bumped wall geometry

parameters required to completely specify the wall geometry of the bumped wall test sections are given in Table 3.1.

All of the bumped wall test sections were used for both pressure and temperature testing. The test sections used the same top and bottom as was used in sfc000. The use of these common pieces fixed the number and location of the thermocouples in the top and bottom. The number and layout of thermocouples in the side walls varied from one bumped wall to the next. The reason for this was the desire to keep the thermocouples either on the flat of a raised bump, the flat of an indented bump, or exactly half way up the sloped edge of a bump. This consistency of positioning was done mainly for machining purposes since drilling thermocouple holes at other

Table 3.1: Values of geometric parameters for bumped wall test sections, lengths in mm

Test Section	H_s	H_2	L_1	L_2	L_4	β (°)
sfc010	25.40	7.11	76.20	17.80	17.80	35
sfc011	25.40	7.11	76.20	17.80	17.80	35
sfc012	25.40	5.08	76.20	23.59	23.59	35
sfc013	25.40	5.08	50.80	10.89	10.89	35

locations would have made it very challenging to not drill through the inside surface of the wall.

The wall geometry of test section sfc010 was identical to the current bumped fin geometry being produced by ATS but scaled up by a factor of 10. Test section sfc010 had 47 thermocouples installed along the centerline of one of the sides. A sectioned view of the thermocouples relative to the bumps for the inlet half of one side is shown in Figure 3.6.

Test section sfc011 had the same bump geometry as sfc010 but did not have continuous bumps along its length. Instead, the bumps were spaced intermittently with flat walled sections between the regions with bumps. A diagram showing the layout of the bumped and flat walled regions can be seen in Figure 3.7. The purpose of the intermittent bumps was to see if the enhanced heat transfer coefficient from the bumped regions would carry over into the flat walled regions. It was hoped that an optimal spacing for the intermittent wall geometry could be found that maximized the amount of heat transfer while reducing the friction factor. There were 32

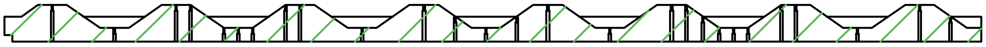

Figure 3.6: Sectioned view of thermocouple holes relative to bumps

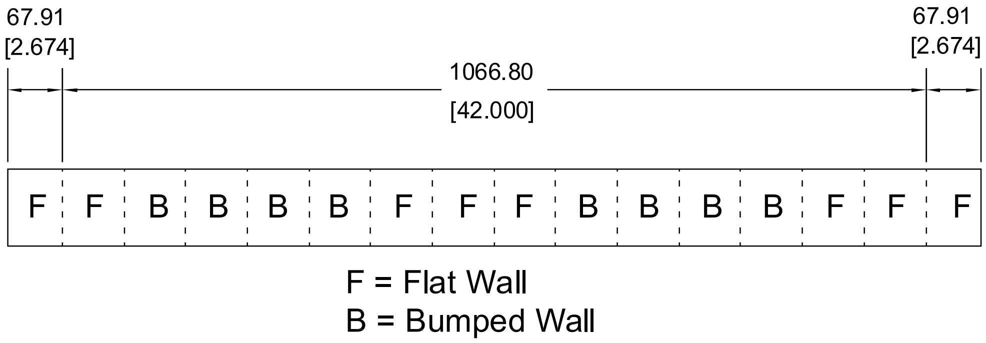

Figure 3.7: Layout of bumped and flat wall geometry for sfc011

thermocouples installed along the centerline of side A. In the bumped regions the thermocouples were again located on the flats of the bumps or exactly half way up the sloped edge.

Test sections sfc012 and sfc013 had bumped wall geometries along their entire lengths that were variations on the geometry of sfc010. Both sfc012 and sfc013 had a shorter bump height than sfc010 resulting in less aggressive bumps. Test section sfc012 had the same bump pitch as sfc010 but had wider bump flats. Test section sfc013 had a shorter bump pitch than sfc010 and smaller bump flats. Both test section sfc012 and sfc013 had 47 thermocouples installed along the centerline of side A. As in all the other bumped test sections, the thermocouples were located on a raised bump flat, indented bump flat, or half way up the sloped edge of a bump.

3.2.5. Longitudinal Vortex Generator Test Sections. Two scaled up test sections were built that had longitudinal vortex generator (LVG) geometries on the side walls. These test sections were designated sfc020 and sfc021. One side wall had the LVG geometry raised from its surface while the opposite side wall had the LVG geometry recessed into its surface. This configuration of the side walls was deemed the most realistic representation of how the LVG geometries would actually be implemented. The cross-section of these test sections was again rectangular when looking at the unenhanced regions. The cross-sectional dimensions and length were identical to the dimensions used for the bumped wall geometries. On both test sections the LVG's were intermittently spaced. The side walls of the test sections were divided into periodic elements that had either LVG's or flat walled profiles as shown in Figure 3.8. The periodic element boundary did not extend across the entire side wall due to manufacturing limitations that would prevent creating LVG's near the edge of the side wall.

A diagram of half of a periodic element (after splitting down the plate centerline) with the geometric notation for the LVG geometries is shown in Figure 3.9. A full periodic element would consist of a pair of LVG's symmetric about the plate centerline. The dimensions of the periodic element shown in Figure 3.9 are $L_s = 76.2$ mm and $L_p = 70.0$ mm. The specific parameters used for the two LVG test sections can be found in Table 3.2.

Both of the test sections with LVG's had 46 thermocouples installed in one of the side walls. Clusters of thermocouples were placed near the LVG's while thermocouples spaced farther apart were installed in the flat walled regions.

As noted from Figure 3.8, the largest number of consecutive columns of LVG's used was two. Dupont et al. [13] found that the intensity of the generated vortices

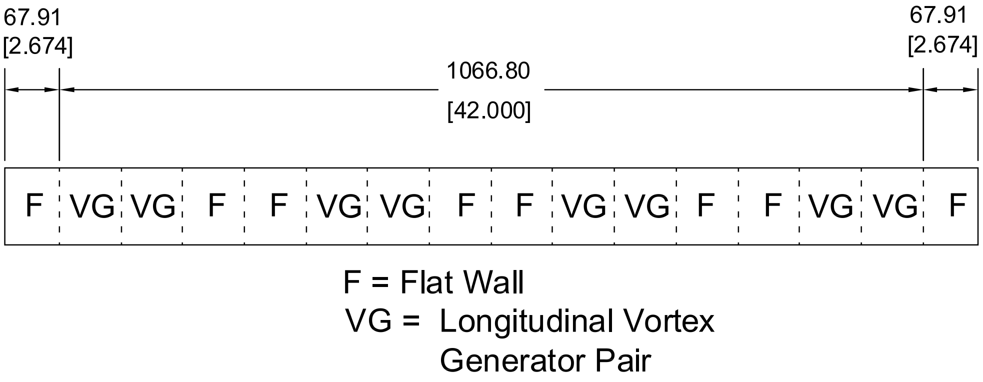

Figure 3.8: Layout of LVG's and flat walled regions

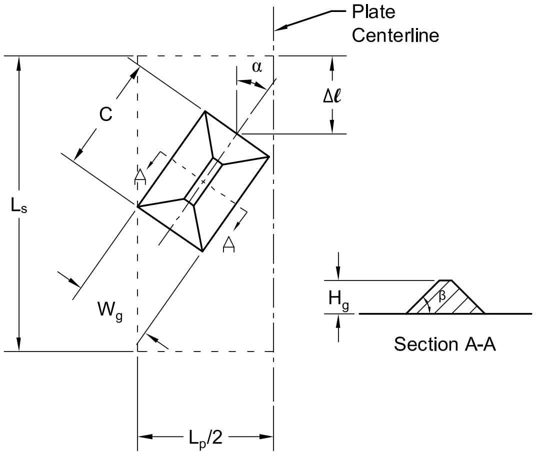

Figure 3.9: Geometric notation for longitudinal vortex generators

Table 3.2: Parameters for LVG geometries, lengths in mm

Test Section	C	W_g	H_g	$\beta(°)$	$\alpha(°)$	Δl
sfc020	30.00	20.19	8.51	45	35	25.81
sfc021	54.99	20.19	8.51	45	15	11.53

was at its maximum value after at most three columns of LVG's. The use of two columns was selected to create the maximum intensity of vortices while not incurring too large of an additional pressure drop. The use of flat walled regions between the LVG's was an attempt to create a surface that increased the heat transfer in the flat walled region more than the friction factor.

The selected angles of attack of 35° and 15° were chosen to take advantage of the results found in [12]. The results in that study showed that a good amount of heat transfer enhancement could be obtained with a relatively low pressure drop penalty for smaller angles of attack.

It should be noted that the design and construction of the LVG test sections was part of the current work, but the experimental testing was beyond the scope of this work. Therefore, no results are presented for the LVG geometries. The experimental results will be available in the future once all experimental tests are completed.

3.2.6. Pressure Taps. Static pressure taps were used in the test section to aid in determining the friction factor. The pressure taps consisted of a 1.70 mm (0.067 in) diameter hole drilled to within 3.18 mm (0.125 in) of the inside face and then a 1.02 mm (0.040 in) diameter hole through the face of the test section. A dimensioned drawing of a pressure tap hole is shown in Figure 3.10. The selected pressure tap dimensions were based on the suggested through hole depth to diameter ratio (L_{pt}/d_{pt}) range of 1.5 to 15 given in [18]. The connection to the pressure taps was accomplished by attaching a 19.05 mm (0.75 in) long piece of 1.59 mm (0.0625 in) outside diameter stainless steel tubing to the 1.70 mm (0.067 in) hole using Loctite 271. Prior to this, a piece of 1.59 mm (0.0625 in) inside diameter copper tubing was attached to the top of the stainless steel tubing using Loctite 271. To the top of the copper tubing, a luer lock hose fitting for 3.18 mm (0.125 in) tubing was attached by pressing it on to the copper. Norprene tubing with 3.18 mm (0.125 in) inside diameter was then connected from the hose fitting to the appropriate port on the pressure manifold using luer lock to hose fittings.

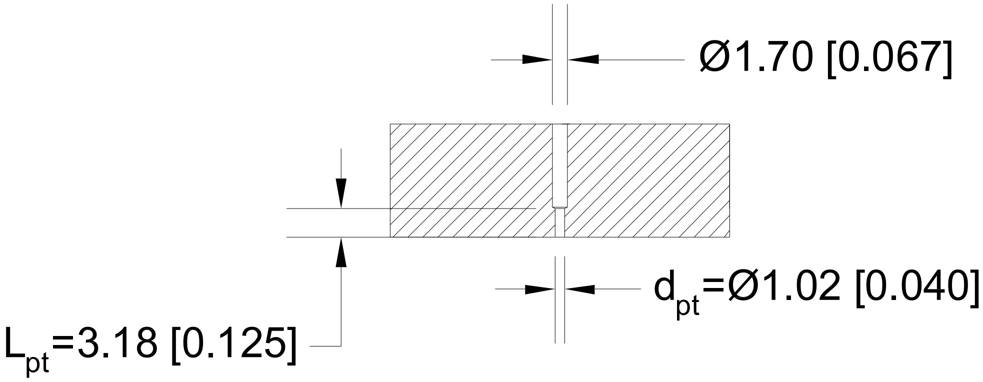

Figure 3.10: Dimensioned drawing of pressure tap

3.2.7. Thermocouple Holes. During the machining operations on each test section, holes were drilled in the test section walls that allowed thermocouples to be installed in the test section. The thermocouple holes were created by first drilling a 1.70 mm (0.067 in) diameter hole to within 3.18 mm (0.125 in) of the inside surface of the test section. Then, a 1.02 mm (0.040 in) diameter hole was drilled to within 0.25 mm (0.010 in) of the inside wall. A dimensioned drawing of a typical thermocouple hole is shown in Figure 3.11.

3.2.8. Test Section Heaters. Heating of the test sections was accomplished using etched foil heaters from Hi-Heat Industries. For the production scale test sections etched foil heaters with mica insulation were used. Mica insulation was required for these heaters due to the heat flux being roughly 31,000 W/m^2 (20 W/in^2) and the heater operating temperature exceeding 200°C. These mica heaters were each sized to output 625 W of heat at 120 V. One heater was attached to the top of the test section and a second heater was attached to the bottom of the test section. All test section heaters were connected to Superior Electric 116C variac transformers to control the input voltage and thus the heater output wattage.

Since the mica insulation became very brittle upon heating for the first time, the mica heaters had to be enclosed in a sandwichlike fashion between aluminum

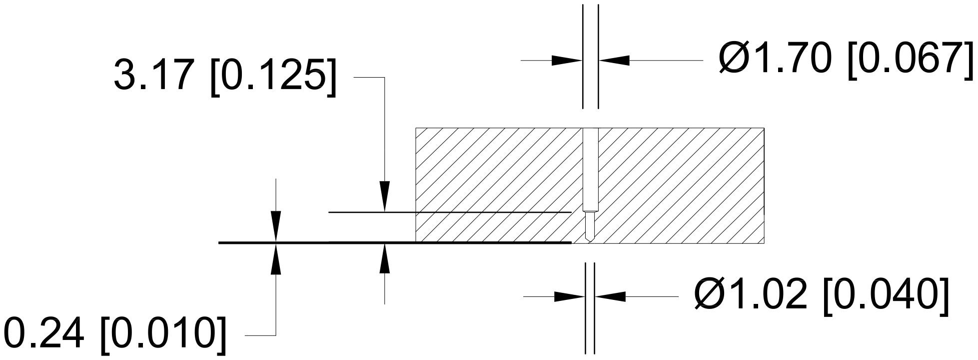

Figure 3.11: Dimensioned drawing of thermocouple hole

plates. A 3.175 mm (0.125 in) aluminum plate was installed under the heater and a 9.525 mm (0.375 in) thick aluminum plate was installed above the heater. In addition, a piece of ceramic paper was placed between the heater and the top plate to aid in attaining uniform pressure on the heater when the sandwich was bolted together. Slots were made in the heater and backing plates to allow thermocouple wires to pass through to the back of the test section. Bolt holes were also drilled in the backing plates to allow them to be permanently bolted together with the mica heater and ceramic paper sandwiched in the middle.

For the scaled up test sections, etched foil heaters were again used but silicone rubber was used as the insulating material. These heaters had a maximum heat flux of 3300 W/m^2 (2.1 W/in^2) and an expected operating temperature below 200°C which allowed for the use of the more flexible and durable silicone rubber insulation. For the top and bottom of the test section, heaters were purchased with an output wattage of 50 W each at 120 V while for each side of the test section a 100 W heater was purchased. In all, four separate heaters were required for the scaled up test sections. All the heaters for the scaled up test section were attached to backing plates made from 1.588 mm (0.0625 in) thick aluminum using RTV silicone. The backing plates and heaters had slots and holes in them that allowed thermocouple wires to pass through to the test section walls and also allowed the heaters to be bolted to the test section. Additionally, a top plate also made from 1.588 mm thick aluminum was bolted on top of the heater and its backing plate to protect the silicon rubber insulation while in use.

3.3. DATA ACQUISITION EQUIPMENT

Data acquisition during the experimental tests was performed using a combination of computer and manual measurement equipment as described in the following sections.

3.3.1. Pressure Measurement. Pressure measurements that were required during testing included differential pressures from one pressure tap to another on the test section, the differential pressure across the orifice flow meter, and gage pressure measurements at various locations. All pressure measurements required during experimental testing were performed using a Dwyer Microtector manometer. This manometer had a differential pressure range from 0 to 498 Pa (0 to 2 in w.g.). The stated accuracy of the manometer was ±0.0623 Pa (±0.00025 in w.g.) which allowed for the measurement of very small differential pressures with reasonable uncertainty. The manometer had two hose barb ports (high and low pressure) to which the sources of pressure were connected. Norprene tubing with an inside diameter of 4.76 mm (0.1875 in) was connected from the outlet of the pressure manifolds to each of the ports on the manometer when differential pressure measurements were being made. For gage pressure measurements, one side of the manometer was left open to the atmosphere while the other was connected to tubing from the pressure manifolds. A diagram of the pressure measurement system can be found in Figure 3.12.

Pressure manifolds were used to control which pressure taps were being used. A high and a low manifold were required so each tap could be connected to either the high or the low pressure side of the Dwyer Microtector manometer. Each pressure tap on the test section was connected to a tee. One branch from the tee ran to the high pressure manifold and the other branch ran to the low pressure manifold. The valves on the manifold allowed the user to select which pressure tap would be the higher pressure tap and which pressure tap would be the lower pressure tap. For any given measurement on the manometer, only one valve on the high pressure manifold was opened and only one valve on the low pressure manifold was opened.

3.3.2. Temperature Measurement. Thermocouples were used to measure the temperature at various locations in the test section. All thermocouples used were purchased from Nanmac Corporation. The thermocouples were made from 30

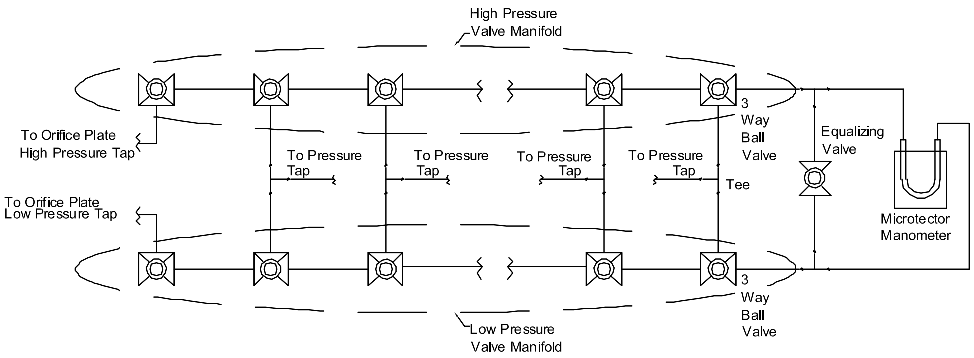

Figure 3.12: Schematic of pressure system

gage wire and were type T (copper/constantan) with extruded Teflon insulation. The extruded Teflon insulation had a maximum temperature rating of 260°C which comfortably exceeded the maximum expected operating temperature of 200°C. The thermocouples were purchased as a spool of insulated wire.

The thermocouples used to make measurements were directly connected to a zone box which allowed multiple thermocouples to reference a single ice point in their measurements. A schematic of the setup is shown in Figure 3.13 The overall system used for temperature measurement was developed by K.S. Benne.

The positive and negative leads of the thermocouples were connected to National Instruments CB-68-LPR connecting blocks which were mounted inside the insulated sheet metal zone boxes. Two CB-68-LPR blocks were required since 80 channels of thermocouple data were collected. The first CB-68-LPR collected data for channels 0-15 and the second CB-68-LPR collected data for channels 16-79. The thermocouples were wired in non reference single ended (NRSE) mode. This mode required that the positive lead (blue wire) be connected to the specific terminal on the block for the channel used to collect data from the thermocouple. All the negative thermocouple leads (red wires) were connected to the AI Sense terminal on the connecting block. In addition, a 110 kΩ resistor was wired between AI Sense and AI

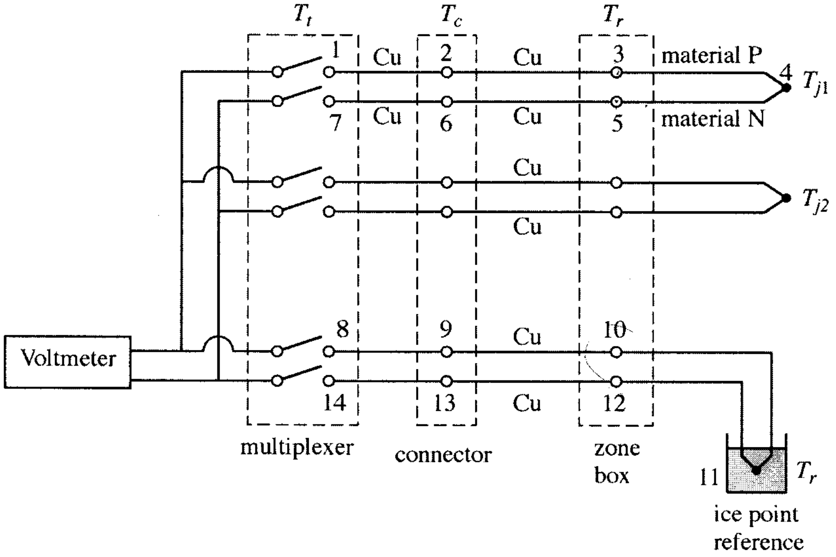

Figure 3.13: Temperature measurement setup

Ground to prevent a build up of charge on the connecting block that could cause the common mode voltage to saturate the amplifier.

An ice bath was made during each test by placing crushed ice in a Dewar flask. The purpose of the ice bath was to provide a reference temperature for the temperature measurements. The ice was crushed to the consistency of snow prior to being placed in the flask. The Dewar flask was first packed with ice and then ice water was poured into the flask until no more water could be added. A tight fitting lid was then placed on the flask with two glass tubes passing through holes in the lid. The glass tubes had been half-filled with WD-40 prior to their insertion. One thermocouple was inserted into each glass tube until the thermocouple bead bottomed in the tube. One of the thermocouples was wired to the first CB-68-LPR connecting block to act as its temperature reference and the second thermocouple in the ice bath was wired to the other CB-68-LPR block.

The connector shown in Figure 3.13 was a set of shielded cables that connected the CB-68-LPR blocks to the data acquisition cards in the computer. The data acquisition cards in the computer contained the multiplexer shown in Figure 3.13. These components are discussed further in Section 3.3.6.

3.3.3. Bulk Temperature Measurement. Measurements of the bulk fluid temperature of the working air were made in the inlet and outlet settling chambers. Temperature measurements were made at various locations across the cross-section to determine the bulk temperature. Sampling trees were made from 0.635 cm (0.25 in) outside diameter tubing with four pieces of 0.318 cm (0.125 in) outside diameter copper tubing 2.54 cm (1.00 in) in length attached orthogonal to the axis of the main tube on alternating sides at locations 1.91, 5.72, 9.53, and 13.34 cm (0.75, 2.25, 3.75, and 5.25 in) from the end. Thermocouples connected in series were attached to the end of each copper tube. The thermocouples were of the same type as those used in the test section.

The bulk temperature measured in the inlet settling chamber was found using two thermocouple trees installed 45.72 cm (18 in) from the test section inlet. Thus, in all eight thermocouples were used to find the inlet bulk temperature. The outlet bulk temperature was measured in the outlet settling chamber at a location 15.24 cm (6 in) from the test section outlet. Again, two trees with four thermocouples each were used to measure the bulk outlet temperature. The inlet bulk temperature was measured at a distance farther from the test section to ensure that any flow disturbance caused by the trees would die out before the test section entrance.

3.3.4. Air Property Measurement Equipment. To find all the properties of the working air in the flow loop, three different measurements were required. These measurements were the absolute pressure, dry bulb temperature, and the relative humidity of the air. The absolute pressure of the working air was found by combining measurements of barometric pressure and gage pressure. The barometric pressure in the room was measured using an Omega EWS-BP-A Barometer which had a stated accuracy of ±1% of its full scale. Gage pressure measurements at the inlet and outlet of the test section were taken using the Dwyer Microtector manometer. The dry bulb temperature and relative humidity were measured using an Omega Digital Temperature/Humidity Pen, model number PTH-1XA. The accuracy of the dry bulb temperature measurements was given as ±1°C and the accuracy of the relative humidity measurements was ±5%.

3.3.5. Heater Wattage. The amount of power delivered to the test section heaters was measured using GW5 watt transducers from Ohio Semitronics wired in series between the variacs and the heaters. The watt transducers had an accuracy of ±0.2% of the reading plus ±0.04% of full scale wattage. A different range was required for the watt transducers used for the regular scale test sections than the scaled up test sections. For the regular scale tests the transducer wattage range was from 0 to 1200 W and for the scaled up tests the range was 0 to 250 W.

A third CB-68-LPR connecting block was used to measure the 0-10 V output signals from the watt transducers. These signals could not be acquired on the same blocks as the thermocouples due to the thermocouple signals having a voltage range 1000 times smaller than the watt transducer signals.

3.3.6. Computer System. Two different PCI data acquisition cards were used in the computer that collected the data. The first card was a National Instruments (NI) 6035E that was used to acquire the data from the watt transducers. The 6035E was capable of collecting data from up to 16 analog channels. The second card was an NI PCI-6225 card that was used to acquire data from all the thermocouples. The PCI-6225 was able to collect data from up to 80 analog inputs. The 6035E was connected to the third CB-68-LPR block using an NI 184749-02 connecting cable. The PCI-6225 had two connecting ports. One was connected to the first CB-68-LPR block using an NI SHC68-68-EPM cable and collected data for channels 0-15 on the card. The second connector on the PCI-6225 was connected to the second CB-68-LPR using a SHC-68-68 cable. This connection transmitted the data for channels 16-79 to the PCI-6225.

Once all connections were made and verified, a LabVIEW virtual instrument (VI) was used to collect data from the data acquisition channels. The user was allowed to specify which channels should be used to collect data. The sampling rate used for all channels on all the tests was 1000 Hz. Once steady state was achieved for the given flow rate of interest, approximately 45 seconds of data was collected. This amount of data was selected to avoid data acquisition files that were very large and to minimize the amount of computational time needed to reduce the raw voltage signals into useful results. When collecting data from all available channels each data acquisition file was roughly 35 MB in size.

3.4. TEST SECTION ASSEMBLY

The two different scale test sections were assembled in different manners. The following sections describe the procedure followed to assemble the test sections.

3.4.1. Thermocouple Construction and Installation. The thermocouple construction and installation procedure is the same for both scales of test sections. To begin the process of making each thermocouple, cut a length of wire 168 cm long from the roll. Then, 75 mm of the brown outer insulation should be removed from one end of the wire and 25 mm of the brown insulation should be removed from the opposite end. The exposed red and blue insulated wires are then stripped to bare wire for a length of 7 mm on both ends of the thermocouple wire. Then, use the Miyachi Unitek resistance thermocouple welder to weld a bead on the end of the wire with 25 mm of the brown insulation removed. After the welding the thermocouple bead, dip the bead in Dow Corning 1-2577 conformal coating to electrically insulate the bead.

The process of installing the thermocouples in the holes begins by filling the holes with Omega Bond 600 cement from Omega Engineering. Use a straight pin and a piece of 1.59 mm (0.0625 in) diameter wire to fill each hole with cement and then press the cement into the hole. Then, dip the thermocouple bead in Omega Bond 600 and insert the bead into the hole until the bead bottoms in the hole. This same installation process should be repeated for all thermocouples. Once all the thermocouples are installed, the Omega Bond 600 cement should be allowed to set for 18-24 hours at room temperature as recommended by the manufacturer. After that time has passed, bake the test section portions with the installed thermocouples at 82°C for 4 hours and then for an additional 4 hours at 104°C as recommended by the manufacturer. The elevated temperature baking helps properly cure the Omega Bond 600 so it can endure elevated temperatures without cracking or flaking.

3.4.2. Production Scale Channel Assembly. After all the thermocouples are installed, the test section is ready to be assembled. Begin the assembly process by gathering all the parts and fasteners required and then follow the steps given below.

1. Slide the side pieces between the top and bottom plate. Position the sides by pressing 3.18 mm (0.125 in) diameter by 12.7 mm (0.5 in) long dowel pins through the holes in the top into the side pieces. The dowel pins should be a slip fit in the top and a press fit in the sides.

2. Route the thermocouple wires through the slots in the top heater plate and then place the top heater on the test section as shown in Figure 3.14. Then do the same for the bottom heater. Make sure the heater lead wires for both heaters are on the same end of the test section.

3. Loosely bolt the heaters to the test section using 1/4”x2.75” bolts in the four corner holes. Place a flat washer under the head of the bolt and use a flat washer, lock washer, and nut on the opposite end.

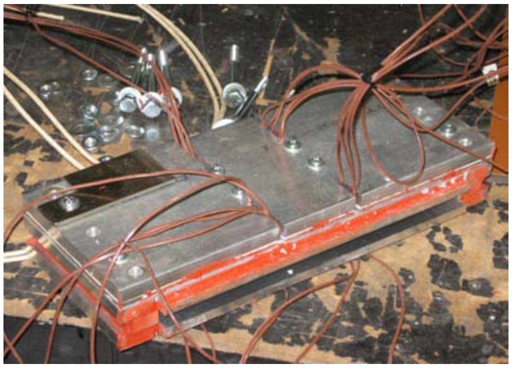

Figure 3.14: Top heater installed on test section

4. Place a piece of phenolic in the center of the heater between the thermocouple wires as shown in Figure 3.15.

5. Lay a steel bar over the piece of phenolic as shown in Figure 3.16. Then repeat placing phenolic and a steel bar on the bottom heater. These phenolic/steel bar hold downs ensure that the center of the heater is firmly held against the test section.

6. Bolt the phenolic/steel bar hold downs to the test section using 1/4”x3 1/2” hex bolts, flat washers, lock washers, and nuts. Tighten securely. Then, tighten the four corner bolts holding the heaters to the test section. Be sure none of

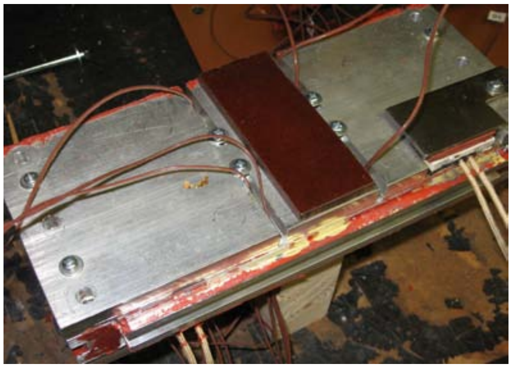

Figure 3.15: Phenolic piece positioned on heater

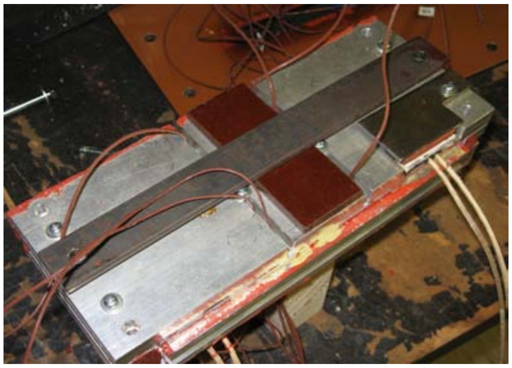

Figure 3.16: Steel bar in place over phenolic

the washers on the corner bolts extend over the edge of the heater. The test section should now appear as shown in Figure 3.17.

7. Seal the seam between the sides and the top and bottom pieces using a bead of RTV silicone along the length of the test section.

8. Attach the inlet phenolic flange to the test section using RTV silicone. The inlet end of the test section should be the end with no heater lead wires. Apply a bead of silicone along the top of the inlet edge of the test section. Fill any gaps between the phenolic and the test section using more silicone. Stand the

Figure 3.17: Heaters completely bolted to test section

assembly on the inlet phenolic flange making sure to set the flange on blocks that do not touch the test section/phenolic joint.

9. Attach the outlet phenolic flange using the same method as for the inlet phenolic flange. Be sure to route the heater lead wires through the cutouts in the outlet phenolic flange. Fill any gaps between the heater lead wires and the cutouts using silicone. The test section should now appear as shown in Figure 3.18. A close up view of the heater lead wires passing through the cutouts can be seen in Figure 3.19.
10. Allow the silicone to dry for 12 hours before moving the assembly.
11. The test section is now ready to have the final assembly steps described in Section 3.4.4 performed.

3.4.3. Scaled Channel Assembly. Once the thermocouples are all installed, cured, and baked, the assembly of the channel can begin by following the steps below.

1. Collect all pieces required for complete assembly of the test section. There should be 10 total pieces to fully assemble each test section.
2. Stand the inlet halves of sides A and B on a flat surface.

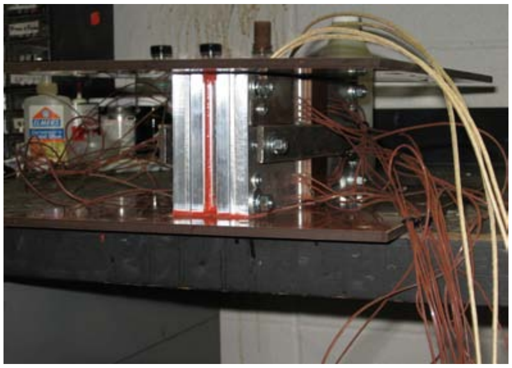

Figure 3.18: Phenolic flange plates attached to test section

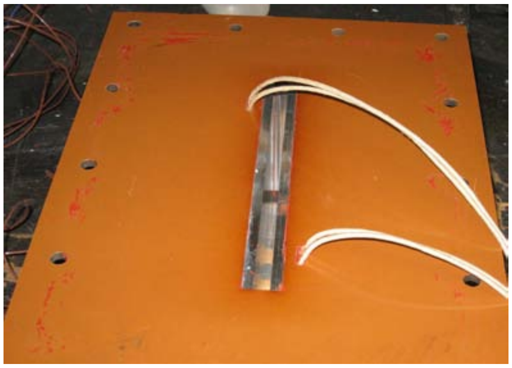

Figure 3.19: Heater lead wires passing through phenolic cutouts

3. Use cyanoacrylate glue to attach ceramic paper to the tops of both pieces as shown in Figure 3.20.

4. Install the inlet third of the top to sides A and B using 8-32x1/2” socket head cap screws (SHCS) as shown in Figure 3.21. Check to ensure that the sides are square to one another by measuring the separation distance at both ends using calipers as shown in Figure 3.22. Also check that the overhang of the top is the same from end to end. This should be checked using calipers as demonstrated in Figure 3.23.

Figure 3.20: Ceramic paper glued to top of sides

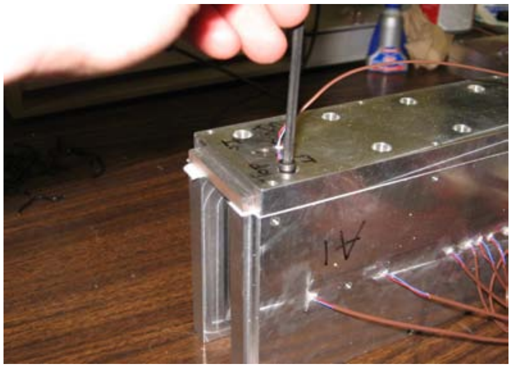

Figure 3.21: Installing top of test section

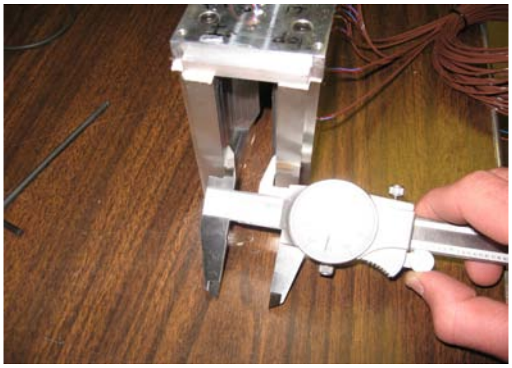

Figure 3.22: Measuring separation distance at inlet

5. Glue ceramic paper to the top side of the outlet halves of sides A and B.

6. Coat both ends of the middle third of the top with Omegatherm 201 paste as shown in Figure 3.24. Also coat the inlet ends of the outlet halves of sides A and B. This paste is used to aid heat transfer between pieces.

7. Align the outlet halves of sides A and B with the inlet halves and then install the middle third of the top using 8-32x1/2” SHCS. Alignment and squareness should again be checked with calipers.

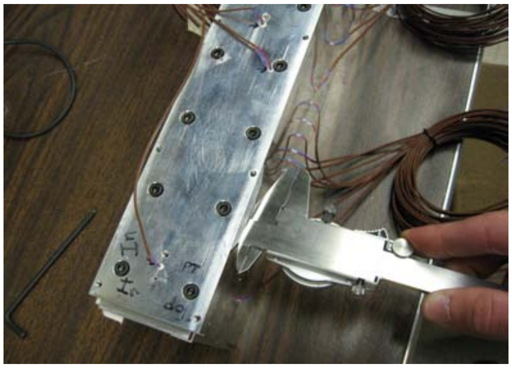

Figure 3.23: Measuring top overhang

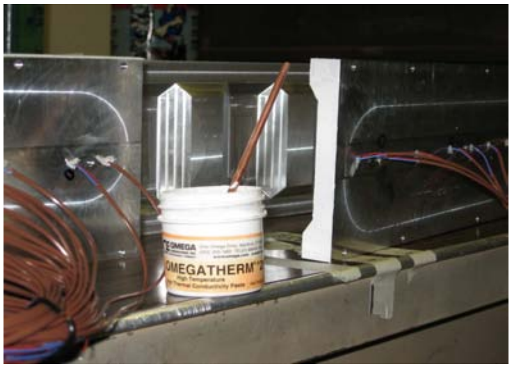

Figure 3.24: Ends of test section coated with Omegatherm paste

8. Install the outlet third of the top using 8-32x1/2" SHCS and again check alignment and squareness of all pieces.

9. Once the top is completely installed, flip the entire assembly over and set the top side on two 2x4 wooden blocks as shown in Figure 3.25. Be sure that the blocks are positioned so thermocouple wires do not get damaged by the test section sitting on them.

10. Glue ceramic paper on the bottom edges of the sides.

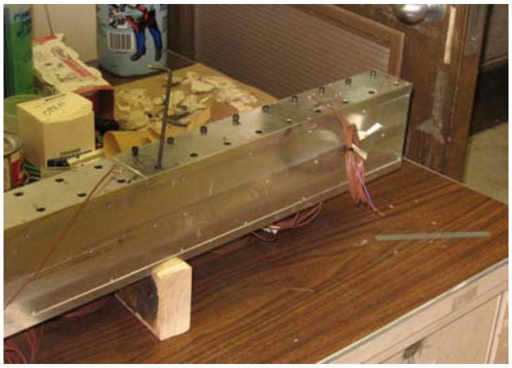

Figure 3.25: Test section flipped for bottom installation

11. Install the bottom side starting with the inlet third and then working toward the outlet. All pieces of the bottom should be installed using 8-32x1/2" SHCS and checked for alignment and squareness. Be sure to coat both ends of the middle third with Omegatherm 201 prior to installation.

12. The silicone rubber heaters with backing plates should be installed next. The heaters can be installed in any convenient order. The heater lead wires should all be kept toward the inlet end of the test section. Details on heater installation are given in the following steps.

13. Guide the thermocouple wires from the bottom side through the slots in the heater and backing plate as shown in Figure 3.26.

14. Attach the bottom heater to the test section using 6-32x1/4" SHCS in the holes on the outside perimeter and 6-32x3/8" SHCS with two #6 flat washers in the holes along the centerline as shown in Figure 3.27. Do not overtighten the bolts or the heater may be damaged. When using the allen wrench only tighten the bolts using the shorter leg for leverage. Do not tighten the bolts using the longer leg for leverage or else heater damage will occur.

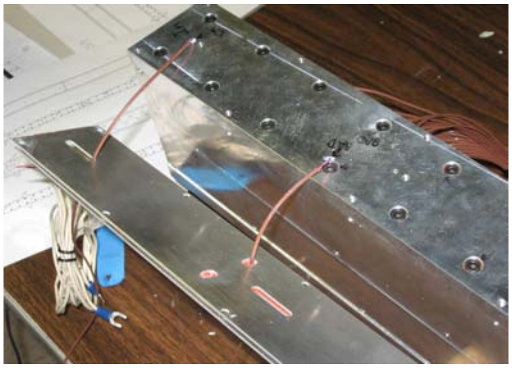

Figure 3.26: Guiding thermocouple wires through heater slots

Figure 3.27: Bolts used to hold heaters in place

15. Flip the test section so side A is up. Rest the test section again on the 2x4 blocks making sure to not smash any thermocouple wires.

16. Attach a heater to side A using the same bolting scheme as for the bottom heater.

17. Continue flipping the test section and installing heaters until all four sides have heaters attached.

18. Select one 6-32x3/8" SHCS on side B (the side without centerline thermocouples) to remove. Replace with a 6-32x1/2" SHCS, #6 flat washer, and ground

wire that will later be attached to the testing stand frame. The installed ground wire is shown in Figure 3.28. This ground wire ensures that if a heater shorts out to the test section the leaking current will safely pass to the frame and trip the GFCI outlet before any harm to the operator can occur.

19. Remove four 6-32x1/4" SHCS from the middle of the top heater. Replace these bolts with four 6-32x3/8" SHCS with #6 washers and wire loops as shown in Figure 3.29. These hooks will be used to securely hold the phenolic flange plates in place.
20. Dry fit the phenolic flanges on both ends of the test section.
21. Pass a rope through the middle flange bolt holes on the sides of each phenolic plate. Tie a knot in the rope on the outside of the plate as shown in Figure 3.30.
22. Tie the other end of the ropes to turnbuckles as shown in Figure 3.31. Then attach the turnbuckles to the wire loops installed in step 19.
23. Adjust the turnbuckles until the phenolic is pulled evenly on to the test section.
24. Loosen the turnbuckles until the phenolic plates can be removed from the test section. Then, remove the phenolic end plates.

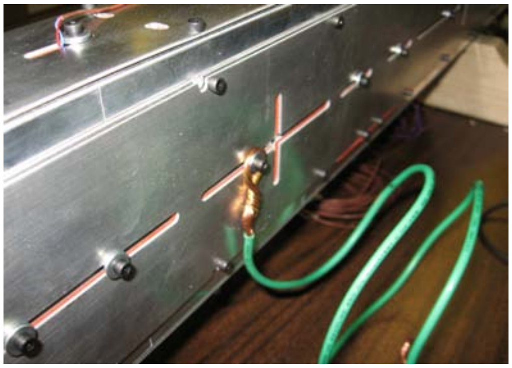

Figure 3.28: Ground wire attached to test section

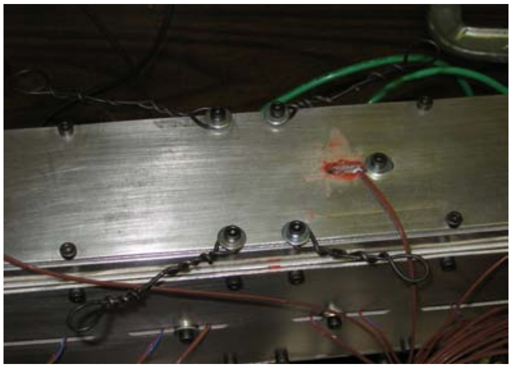

Figure 3.29: Wire hooks attached to top

Figure 3.30: Knots tied outside of phenolic flange

25. Apply RTV silicone to the tab on the test section and the end face on both ends of the test section as shown in Figure 3.32.

26. Install the phenolic end plates on the test section and secure in place by evenly tightening the turnbuckles.

27. Add silicone around the test section to phenolic seam to fill any voids as shown in Figure 3.33.

28. Allow the silicone to dry for at least 12 hours before moving the test section.

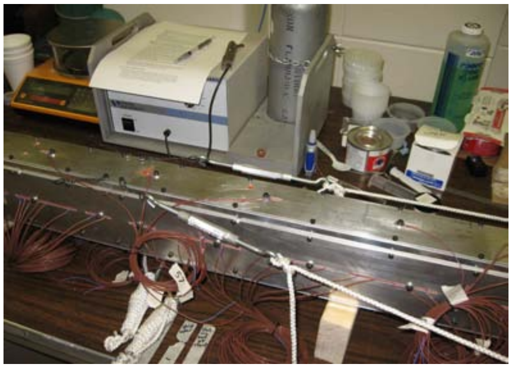

Figure 3.31: Turnbuckles used to tighten phenolic flange to test section

Figure 3.32: RTV silicone applied to test section

29. Remove the ropes and turnbuckles after the silicone has dried. Also, replace the (4) 6-32x3/8" SHCS with the original 6-32x1/4" SHCS in the top of the test section after removing the wire loops.

3.4.4. Final Assembly Steps. The steps in this section can be completed while waiting for the silicone to dry, as long as the test section is not moved.

1. Pressure taps should be installed according to the procedure outlined in Section 3.2.6. The pressure taps should only be installed after the heaters are attached to the test section or else the hose barb on the pressure taps will prevent the heater from being installed.

Figure 3.33: Silicone added to fill any voids

2. Labels should be attached to the thermocouple wires to aid in connecting them to the correct channels on the CB-68-LPR connecting blocks. A diagram should be made showing the number given to each thermocouple and its location on the test section. The best position for the labels is 27.9 cm (11 in) from the end that connects to the CB-68-LPR.

3. The thermocouple wires should then be bundled together into groups of five to ten wires. Bundling the wires helps keep them organized and eases the job of finding individual wires when wiring them to the connecting block.

4. One thermocouple wire should be selected to connect to the heater control box. This thermocouple should be selected from either the top or the side and be located near the outlet of the test section. This thermocouple needs to have a standard size Omega thermocouple connector attached to its end so it can be plugged into the control box.

3.5. ASSEMBLED TEST SECTION INSTALLATION

Once the test section is fulled assembled it is ready to be installed in the flow loop. The same procedure should be followed for both scales of test sections.

1. Position the inlet and outlet flanges on the settling chambers so they are separated by the length of the test section plus at least 7.62 cm (3 in).
2. Move the assembled test section and place it on supports that roughly align it with the end flanges on the settling chambers.
3. Since the outlet settling chamber position is fixed, the test section should first be aligned and leveled to match the flange plate on the outlet settling chamber as shown in Figures 3.34 and 3.35.
4. Level the test section from end to end and side to side.
5. Ensure that the rubber gasket is in place between the aluminum flange plate and the phenolic flange plate.
6. For the production scale test sections, the heater lead wires should be routed through the hole in the top of the outlet settling chamber. For the scaled up test sections, this step is not necessary.
7. Connect the test section to the outlet settling chamber by installing 5/16"x1 1/4" bolts in the flange connection as shown in Figure 3.36.

Figure 3.34: Aligning test section with outlet settling chamber flange

Figure 3.35: Leveling phenolic flange to match aluminum flange

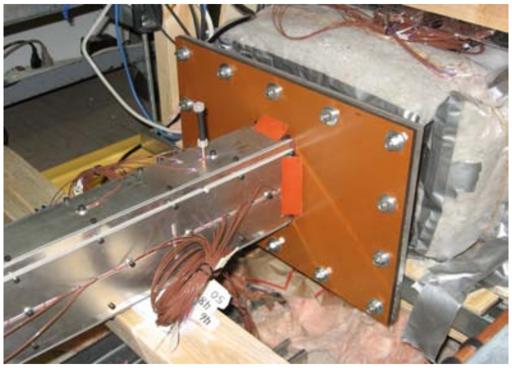

Figure 3.36: Bolted flange connection

8. Adjust the inlet settling chamber so the aluminum flange plate is aligned and level with the phenolic inlet plate on the test section.
9. Check to make sure the rubber gasket is between the aluminum flange and the phenolic flange.
10. Attach the inlet settling chamber to the test section by installing 5/16”x1 1/4” bolts in the flange connection.

11. The test section can now be insulated. Begin by covering the entire test section in a layer of mineral wool insulation. The mineral wool should be secured using wire staples to hold the pieces together as seen in Figure 3.37.

12. Cover the mineral wool insulation with two layers of fiberglass insulation. The first layer should run longways while the second layer should wrap around the test section. Loosely secure the fiberglass using rope ties to hold each layer in place. Make sure all the thermocouple wires, heater lead wires, and pressure lines extend through the fiberglass.

13. Reinsulate the settling chambers making sure to place a layer of mineral wool insulation directly behind the aluminum flange plates.

14. Connect the clamp together ducting to the inlet settling chamber.

15. Move the instrument platform so it is centered over the test section.

16. Connect the ground wire, which was attached to the test section earlier, to one of the bolts used to hold the instrument platform in place.

17. Wire the thermocouple wires to the appropriate channels on the CB-68-LPR connecting blocks.

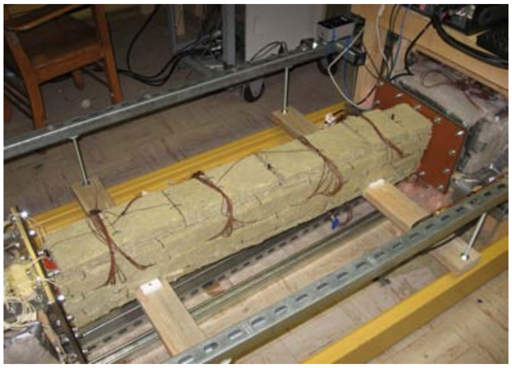

Figure 3.37: Mineral wool insulation on test section

18. The thermocouples should be checked to determine if any of the thermocouple beads are shorted to the aluminum plates of the test section. If any of the thermocouples are shorted to the plate, all the thermocouple signals will have a large amount of noise. The easiest way to check all the thermocouples is to measure the resistance between the AI Sense terminal on the CB-68-LPR and the test frame using a multimeter. If the resistance is not infinite, then at least one thermocouple is shorted to the test section. The shorted thermocouple(s) can be found by checking the resistance between the positive terminal of each thermocouple and the test frame. The thermocouples that are shorted will have a resistance much lower (usually under 10 Ω) than the other thermocouples. All shorted thermocouples should be disconnected from the CB-68-LPR and a piece of wire should be connected between the positive and negative terminals on the connecting block to prevent noise from being picked up by the open terminals. Some thermocouples may short to the plate as a result of operation. A check should be made that no new thermocouples have shorted to the plate before collecting each set of data. One sign that a thermocouple has shorted to the plate is if the range of variation in the plate temperatures is greater than 1°C for a given thermocouple.

19. Connect the pressure lines from the pressure taps and the flow meter to the corresponding ports on the pressure manifolds.

20. Connect the heater lead wires to the proper terminals on the watt transducers. For the scaled up test sections the top and bottom heaters should be wired to one of the 250 W full scale transducers and the two sides should be wired to the other 250 W full scale transducer. When testing a regular scale test section the top heater should be wired to one 1200 W full scale transducer and the bottom heater should be wired to the other 1200 W full scale transducer. Also, check

that the watt transducer signal wires are still connected to the proper channels on the appropriate CB-68-LPR.

21. Connect the data cables from the CB-68-LPR connecting blocks to the appropriate cards on the computer that will be used for data acquisition.
22. Run the power cords from the watt transducers and variacs to the outlets. The variacs should only be plugged into GFCI outlets to protect the operator in case of a shorted out heater.
23. The test section is now ready for testing according to the procedures outlined in Sections 3.8.2 and 3.8.3.

3.6. TEST SECTION DISASSEMBLY

The process of removing a test section once all testing is completed should follow the steps listed below.

1. Remove the insulation from the ducting just upstream of the inlet settling chamber. The ducting should then be disconnected from the settling chamber by removing the clamp.
2. Remove the insulation from the settling chambers.
3. All computer cables, thermocouples, heater wires, power cords, and pressure tap lines should be disconnected.
4. Move the instrument platform out of the way.
5. Remove the insulation from the test section and place it in labeled boxes for use on the next test section.
6. Remove the flange bolts first from the outlet flange and then from the inlet flange.

7. Lift the test section from the loop and place it on 2x4 wooden supports to keep the weight off the phenolic flange plates.
8. Remove the phenolic end plates by carefully applying even pressure and working around the connection.
9. Remove the bolts attaching the heaters to the test section. Once the bolts are removed the heaters should be removed and placed in a safe location.
10. Disassemble the test section components. Any pieces that will be reused should be cleaned to remove any Omegatherm or RTV silicone that may be on them.

3.7. VALIDATION TESTS

Two different tests were conducted prior to collecting any experimental data to make sure the flow loop was functioning properly. These tests are described in the following sections.

3.7.1. Leakage Test. The first test that was performed was an air leakage test. The purpose of the air leakage test was to determine if any air was leaking from or to the loop between the inlet to the test section and the orifice flow meter. This check was important due to the assumption that all the air passing through the flow meter had passed through the test section. If this was not the case, then the flow rate measured by the flow meter could not be used in calculations for the test section.

Measurement of the flow rate at the inlet of the test section was accomplished by performing a pitot tube traverse of the inlet settling chamber cross-section 19.05 mm (0.750 in) upstream of the test section inlet. The pitot tube selected for use was a Dwyer 167-6-CF. The flow rate used for this test was at the high end of the range expected during experimental testing. This flow rate was selected for two reasons. First, it gave the largest velocity pressure measurements from the pitot tube (and thus the smallest uncertainty in the measurements) and second the leakage of air to or from the loop would be the worst at the highest flow rate.

Initially a traversing grid was set up that split the cross-section into 16 equal areas and measured the flow rate at the centroid of each of the areas. However this grid resulted in very coarse measurements and measurements that were inconclusive. After referring to [19], the method outlined in that standard was adopted for the creation of the traversing grid. The resulting grid had 24 sampling points laid out using the log Tchebycheff rule. The results from these tests showed that within the uncertainty of the methods and equipment used, the flow rate at the inlet of the test section was identical to the flow rate at the orifice flow meter.

3.7.2. Flow Visualization. Validating the performance of the flow conditioning components upstream and downstream of the test section was another important item to consider before performing experiments. Flow visualization was used in the Plexiglas settling chambers to observe the air flow patterns in the settling chambers. Visualization was performed at both the lowest and the highest flow rates expected during testing. For the low flow rate, smoke was used as the visualization medium. The smoke was generated by dripping liquid smoke onto a heated aluminum plate at the intake of the inlet settling chamber. For the high flow rate the liquid smoke method did not produce a large enough volume of smoke to visualize so dry ice was used. A very large volume of sublimating carbon dioxide was produced by placing a chunk of dry ice in a hot pot with boiling water.

At both the low and high flow rate the flow visualization test confirmed that the flow conditioning elements were performing as designed. The screens in the inlet settling chamber helped create a uniform velocity profile with minimal disturbances and the honeycomb did a very good job of straightening the flow. In addition, it was found that the flow disturbance caused by the bulk temperature trees in the inlet settling chamber had completely died out long before the test section inlet. In the outlet settling chamber it was found that the flow jetted out from the test section and the jet persisted nearly all the way through the settling chamber. The screens did diffuse the jet as it passed through them, but the diffusion was not very pronounced for either flow rate. Large recirculation zones were observed outside of the jet in the outlet settling chamber. For the high flow rate the speed of the recirculation was very quick and resulted in good mixing of the air in the chamber. For the low flow rate the recirculation was very slow and the air did not seem to mix very well outside of the jet.

3.8. EXPERIMENTAL TESTING PROCEDURES

The procedures to collect experimental data are given in the following sections. The first thing that should be done for all tests is to set the flow rate to the desired value. Measurements of barometric pressure, dry bulb temperature, and relative humidity of the room air should be made and used to calculate the differential pressures across the orifice plate for the flow rates of interest. Coarse adjustments of the flow rate can be made by using the blower motor speed control and fine adjustments can be made using the gate valve near the outlet of the blower. The magnehelic gage near the blower, which indicates orifice plate differential pressure, can be used to roughly adjust the flow rate. The Microtector manometer should be used to verify the flow rate.

The variacs should then be used to adjust the heater output wattage to the desired level. The heater wattage should be based on the desired bulk temperature rise from inlet to outlet of the test section. On the scaled up test sections the top and bottom heater wattage should be adjusted until the temperatures measured by the offset thermocouples near the corners match for the top/bottom and the sides. A good starting point is to input 80% of the total desired heater wattage through the side heaters and the remaining 20% through the top and bottom heaters. For all tests, these setttings ensured that the temperature difference between components was 1°C or less. If a test section inlet temperature above room temperature is desired, then the dampers should be adjusted as described in Section 3.8.1 below, otherwise skip to Section 3.8.2.

3.8.1. Hybrid Loop Operation.

The air flow loop was designed so it could be operated as a purely closed loop, purely open loop, or a hybrid of the two types. To operate in any of these modes, the dampers were adjusted to the proper setting for the desired operation. A drawing of the dampers used to control the flow through different portions of the loop is shown in Figure 3.38.

For start up operation of the loop, the dampers should be adjusted so the loop is a closed loop. For closed loop operation, both dampers at the HRV should be closed, the bleed off cap installed, and the bypass damper opened. For open loop operation, the HRV intake and exhaust dampers are opened and the bypass damper is closed. Depending on the desired temperature at the test section inlet the bleed off cap could be removed and the bleed off damper is used to control the flow of air not passing through the HRV. By positioning dampers in positions between fully opened and fully closed, the flow loop can be operated in a hybrid mode that is not purely open or closed loop.

3.8.2. Pressure Testing.

Measurements of the differential pressure between pressure taps in the test section were used to calculate the friction factor. The steps below describe the procedure for pressure testing.

1. Wait for thermal steady state to be achieved. Thermal steady state is achieved when the difference in the bulk temperature from the inlet to outlet is changing by less than 0.1°C over a 30 minute time span. It should also be checked that there is no long term trend up or down in the bulk temperature difference.

2. Print a blank pressure data sheet and fill in the identifying information at the top.

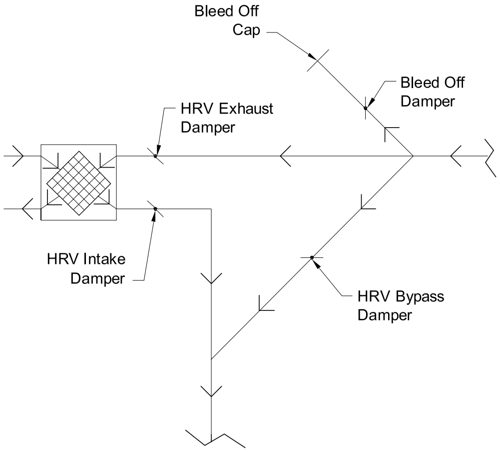

Figure 3.38: Control dampers in loop

3. Measure and record the voltage output by the barometer using a multimeter.
4. Measure and record the room air dry bulb temperature and relative humidity using the thermo-hygrometer pen.
5. Use the Microtector manometer to measure and record the orifice plate differential pressure. Four readings should be made. To take these readings the two valves on the pressure manifold labeled FM should be opened and the equalizing ball valve between the manifolds should be closed.
6. Measure and record the gauge pressure at the first and last pressure taps and also the gauge pressure at the flow meter using the Microtector. The gage pressure measurements should be made by connecting a pressure line to only one side of the Microtector. The other side should be left open to the atmosphere. Then, the valve on the pressure manifold for the location of interest should be opened and the equalizing ball valve closed. Four reading should be made for each pressure.

7. Use the Microtector to measure and record the differential pressure between pressure taps in the test section. Measurement of the differential pressure is performed by opening the valve for the upstream pressure tap on the high side of the pressure manifold and opening the valve for the downstream pressure tap on the low side of the pressure manifold. Then, the equalizing ball valve between manifolds should be closed. Four measurements should be made for each differential pressure.
8. When finished measuring the differential pressures from the pressure taps, measure and record the same items as measured in steps 3, 4, 5, and 6.
9. Use LabVIEW to acquire 45 seconds of data. Data should be collected from all channels.

3.8.3. Temperature Testing. Temperature testing should normally be done immediately after pressure testing. Since the time required to reach steady state is very long, it is much more efficient to take both pressure and temperature data once at steady state.

1. If not taking temperature measurements immediately after pressure measurements, wait for thermal steady state. The same guidelines given for pressure testing should be used to determine when steady state has been reached.
2. Print a temperature data sheet and fill in the identifying information at the top.
3. Measure and record the output voltage from the barometer using a multimeter.
4. Use the thermo-hygrometer pen to measure and record the room air dry bulb temperature and relative humidity.

5. The orifice plate differential pressure and the gage pressure at the orifice plate should be measured using the Microtector. The same method used in Section 3.8.2 steps 5 and 6 should again be used for these measurements.
6. Use LabVIEW to record 45 seconds of data from all channels.
7. Record the additional information asked for at the bottom of the data sheet for future reference.

4. EXPERIMENTAL RESULTS AND DISCUSSION

4.1. DATA REDUCTION

A PV-Wave program was written to reduce the raw data collected during experimentation into useful results. The following sections describe the procedure and equations that were used in the data reduction.

4.1.1. Air Property Calculations. After measurements were made of the dry bulb temperature and relative humidity of the air in the lab, the humidity ratio was determined. It was then assumed that the humidity ratio was the same for the working air in the flow loop as the lab air. This assumption was valid because the working air in the flow loop was being pulled in from the lab and no humidification or dehumidification was being performed. The dry bulb temperature of the working air was directly measured using the bulk temperature thermocouples. In addition, the gage pressure at various locations in the test section was measured using the Microtector manometer. The gage pressure was used along with the atmospheric pressure measured with the barometer to determine the absolute pressure of the working fluid. Once these three properties were known, (humidity ratio, dry bulb temperature, and absolute pressure) all other properties were calculated from psychrometric relationships.

The compressibility factor, Z, was found using Eq. (11).

$$Z = 1 + B'_{mix}P + C'_{mix}P^2 \tag{11}$$

The virial coefficients B'_{mix} and C'_{mix} were calculated using information found in [20] and [21]. The dynamic viscosity of the air, μ_m, was found using the Sutherland formula shown in Eq. (12) with information from [22].

$$\mu_m = \frac{\mu_w}{1 + G_{w,a}\frac{X_a}{X_w}} + \frac{\mu_a}{1 + G_{a,w}\frac{X_w}{X_a}} \tag{12}$$

In Eq. (12), the subscript w designated properties for saturated water vapor, the subscript a was for properties of dry air and X_i was the mole fraction of component i. The values of the viscosity constants ($G_{w,a}$ and $G_{a,w}$) were found from relationships given in [22].

The density of the working air was determined at all points of interest using Eq. (13) found in [23].

$$\rho = \frac{PM_a}{RTZ}\left(1 - \left(1 - \frac{18.0152}{M_a}\right)\frac{\phi}{100}\frac{f_e e_s}{P}\right) \tag{13}$$

In Eq. (13), P was the absolute pressure, M_a was the molar mass of air assumed to be 28.963 g/mol, R was the universal gas constant, T was the absolute temperature, Z was the compressibility factor, ϕ was the relative humidity, f_e was the enhancement factor, and e_s was the saturated water vapor pressure. The values of all these variables were evaluated at the measured conditions using information from [20], [21], [23], and [24].

The enthalpy of the air was calculated from the relationship shown in Eq. (14) from [14].

$$h_{da} = T + W\left(2501 + 1.805T\right) \tag{14}$$

In Eq. (14), T was the dry bulb temperature and W was the humidity ratio. The resulting enthalpy has units of $\frac{\text{kJ}}{\text{kg}_{dry\ air}}$. This enthalpy relationship technically only applies at standard atmospheric pressure but due to all testing being done at pressures very close to the standard, the error introduced was negligible.

Thermal conductivity of the air was found using Eq. (15) from [22].

$$k_m = \frac{k_w}{1 + G_{w,a}\frac{X_a}{X_w}} + \frac{k_a}{1 + G_{a,w}\frac{X_w}{X_a}} \tag{15}$$

In Eq. (15) the subscript w again designated properties of saturated water vapor, the subscript a was used for properties of dry air, $G_{a,w}$ and $G_{w,a}$ were the same as the viscosity constants used in Eq. (12), and X_i again designated the mole fraction of component i of the mixture.

4.1.2. Flow Rate Calculation. The volumetric flow rate through the flow loop was found using the method outlined by Miller [15]. A program was written that required input of the following measurements: duct inside diameter, orifice bore diameter, absolute pressure at the high pressure tap of the orifice, dry bulb temperature, relative humidity, and orifice plate differential pressure. These inputs were used to calculate the compressibility factor, dynamic viscosity, and density of the air using the methods described earlier.

The volumetric flow rate, $\dot{V}$, was found using Eq. (16) from [15].

$$\dot{V} = F_{EL} F_M N_{vp} \frac{C_D d^2}{\sqrt{1-(d/D)^4}} \frac{Y_1}{\sqrt{\rho_{f1}}} \sqrt{h_w} \tag{16}$$

In Eq. (16) F_{EL} was an elevation correction factor, F_M was a manometer correction factor, N_{vp} was a units conversion factor, C_D was the discharge coefficient for the quadrant orifice plate, d was the orifice bore diameter, D was the duct inside diameter, Y_1 was the gas expansion factor, ρ_{f1} was the density at the high pressure tap of the orifice plate, and h_w was the measured differential pressure across the orifice plate.

Once the volumetric flow rate was known from Eq. (16), the mass flow rate was found by multiplying the volumetric flow rate by the density at the high pressure tap of the flow meter (ρ_{f1}).

4.1.3. Barometric Pressure. The voltage output by the barometer was used to calculate the barometric pressure based on information provided by Omega Engineering. A table of output voltage and corresponding barometric pressure was provided. A curve fit was made to this information which resulted in finding a nearly perfect linear relationship between output voltage and barometric pressure as shown in Eq. (17).

$$P = 9518V_b + 60888 \tag{17}$$

In Eq. (17), P was the barometric pressure in Pa and V_b was the barometer output voltage in V.

4.1.4. Temperature. Thermocouples can only measure temperature differences and a known reference temperature is required to find absolute temperature when using thermocouples. For the temperature measurement system used in the tests, the ice bath acted as the known reference temperature (0°C).

The raw data collected from each thermocouple installed in the test section was a voltage that corresponded to the temperature difference between the zone box and the location of the thermocouple bead. This voltage was designated E_{T_r,T_j}. However, to be able to use the standard relationships between voltage and temperature the voltage between the thermocouple bead and the ice bath at 0°C was needed. Thus, it was necessary to know the voltage that corresponded to the temperature difference between the zone box and the ice bath. This voltage was found from the thermocouple that was wired to each connecting block with its bead placed in the ice bath and was designated $E_{T_r,0}$. The resulting equation that gave the voltage difference between each thermocouple bead and the ice bath (designated E_{0,T_j}) is shown as Eq. (18).

$$E_{0,T_j} = E_{T_r,T_j} - E_{T_r,0} \tag{18}$$

Once E_{0,T_j} was known, it was converted to microvolts and plugged into a polynomial relating voltage and temperature for a type T thermocouple. The polynomial used was found in [25] and is given as Eq. (19).

$$\begin{aligned} T = 2.5928\text{x}10^{-2}E_{0,T_j} - 7.602961\text{x}10^{-7}\left(E_{0,T_j}\right)^2 \\ + 4.637791\text{x}10^{-11}\left(E_{0,T_j}\right)^3 - 2.165394\text{x}10^{-15}\left(E_{0,T_j}\right)^4 \\ + 6.048144\text{x}10^{-20}\left(E_{0,T_j}\right)^5 - 7.293422\text{x}10^{-25}\left(E_{0,T_j}\right)^6 \end{aligned} \quad (19)$$

In Eq. (19) T had units of °C and E_{0,T_j} had units of μV.

The thermocouples used to measure bulk temperature were connected differently than the other thermocouples installed in the test section. The bulk temperature thermocouples on each tree were wired in series resulting in four thermocouples per tree in series. The raw voltage measured for each series set of thermocouples was the sum of the voltages sensed by the four thermocouples and was designated $E_{T_r,T_{sum}}$. Thus, the equation used to find the voltage corresponding to the average temperature difference between each thermocouple tree and the ice bath was different from the equation used for the other thermocouples. The equation to find E_{0,T_j} for the bulk temperature measurements is shown in Eq. (20).

$$E_{0,T_j} = \frac{E_{T_r,T_{sum}} - 4E_{T_r,0}}{4} \quad (20)$$

The resulting value for E_{0,T_j} was then plugged in Eq. (19) to find the average temperature for each bulk temperature tree.

4.1.5. Fanning Friction Factor. The Fanning friction factor was calculated to allow the frictional losses to be compared between test sections. The formula used to calculate friction factor is shown in Eq. (21).

$$C_f = \frac{\Delta P}{2\left(\frac{L}{D_h}\right)\rho V^2} \quad (21)$$

The value of ΔP in Eq. (21) was the differential pressure measured between pressure taps using the Microtector manometer. The axial distance between pressure taps was used for L. The density, ρ, was found at flowing conditions using Eq. (13) and the mean velocity, V, was found by dividing the mass flow rate by the channel cross-sectional area and density.

The length averaged friction factor ($C_{f,m}$)was the most useful result for many of the tests. The value of $C_{f,m}$ was calculated using Eq. (22) shown below.

$$C_{f,m} = \frac{1}{L}\int_0^L C_f dx \tag{22}$$

For many of the tests, the length averaged friction factor was the only result that could be obtained because of the very small pressure drops along the length of the channel.

4.1.6. Heat Transfer. The expression for the local heat transfer coefficient at a given location on the test section was found by starting with an energy balance at the test section wall/fluid interface. At the interface, the amount of heat conducted through the aluminum test section wall ($\dot{Q}_{cond}$) had to equal the amount of heat convected away by the fluid ($\dot{Q}_{conv}$) due to conservation of energy. This is expressed in Eq. (23).

$$\dot{Q}_{cond} = \dot{Q}_{conv} \tag{23}$$

It was also known from Newton's law of cooling that $\dot{Q}_{conv} = hA\left(T_w - T_b\right)$ where h was the local heat transfer coefficient, A was the area, T_w was the local wall temperature, and T_b was the fluid bulk temperature at the location of interest. Since the area for both modes of heat transfer was equal, the area was divided from both sides of Eq. (23) to arrive at Eq. (24).

$$\dot{q_w}'' = h\left(T_w - T_b\right) \tag{24}$$

In Eq. (24) $\dot{q_w}''$ was the local wall heat flux on the inside of the wall. Then, Eq. (24) was solved for h to arrive at the equation for local heat transfer coefficient. The result of this calculation is shown in Eq. (25).

$$h = \frac{\dot{q_w}''}{T_w - T_b} \tag{25}$$

The local wall heat flux was not constant along the length but rather varied from one location to the next. On the back side of the wall, where the heaters were attached, there was a constant heat flux ($\dot{q_h}''$). However, the good thermal conductivity of the aluminum wall and the varying bulk fluid temperature on the inside of the test section caused the heat flux on the inside of the wall to be higher near the inlet of the test section than at the outlet end. Thus, a conjugate wall problem accounting for the conductivity of the wall material and the convection to the fluid had to be solved to determine the heat flux at each location. The setup for the conjugate wall problem is shown in Figure 4.1. In Figure 4.1, the heater heat flux ($\dot{q}_h''$) was assumed to be uniform along the length and was determined as shown in Eq. (26).

$$\dot{q}_h'' = \eta_e \frac{\dot{W}_e}{A} \tag{26}$$

The conjugate wall problem was solved numerically by imposing a constant wall heat flux of $\dot{q_h}''$ on the outside of the wall and heat transfer coefficient and bulk temperature distributions that varied with position on the inside of the wall. A generic functional form for the variation of heat transfer coefficient with position was used. The parameters in the function were varied until the difference between the numerically predicted inside wall temperature and the wall temperature measured with the thermocouples was minimized. The resulting equation for heat transfer coefficient represented the actual distribution for the wall.

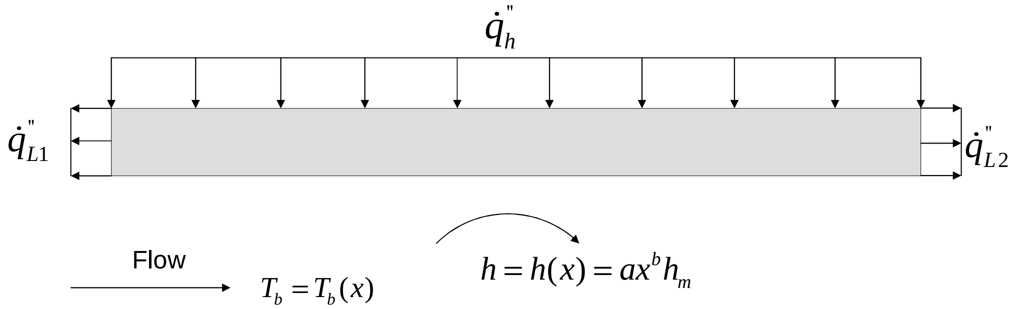

Figure 4.1: Conjugate wall problem setup

Initially, computations were performed with the temperature specified on the inside wall from a curve fit to the temperatures measured by the thermocouples. However, this boundary condition was found to be too rigid and caused numerical instabilities and divergence of the results. The difficulties found when using a specified wall temperature distribution were likely due to the curve fit of the wall temperature not accurately representing the temperature near the ends of the wall. The nearest thermocouples were over 2.5 cm from the end of the wall and were not able to fully capture the end effects. More thermocouples would have been needed closer to the ends to have an accurate curve fit in that region of the wall.

Once the local heat transfer coefficient was found at all locations along the wall, the length averaged heat transfer coefficient (h_m) was found as shown in Eq. (27).

$$h_m = \frac{1}{L}\int_0^L h \; dx \tag{27}$$

The local Nusselt number was calculated from its definition as shown in Eq. (28).

$$\mathrm{Nu} = \frac{hD_h}{k} \tag{28}$$

Additionally, the length averaged Nusselt number (Nu_m) was found using the expression shown in Eq. (29).

$$\mathrm{Nu}_m = \frac{1}{L}\int_0^L \mathrm{Nu}\; dx \tag{29}$$

The local Stanton number was another dimensionless number of interest and was found using Eq. (30).

$$\mathrm{St} = \frac{\mathrm{Nu}}{\mathrm{RePr}} \tag{30}$$

The length averaged Stanton number (St_m) was found using the same equation as the local Stanton number except Nu_m was used instead of Nu. The local Colburn j factor was found using Eq. (31).

$$j = \mathrm{StPr}^{2/3} \tag{31}$$

The length averaged Colburn j factor (j_m) was found by using St_m instead of St in Eq. (31).

4.2. FANNING FRICTION FACTOR RESULTS

Once the data reduction code had been run on the experimental data the Fanning friction factor was one of the resulting pieces of information for each test section. An uncertainty analysis was performed that found the typical uncertainty in the Fanning friction factor to be 10% or less. For the rest of this document any time the words friction factor are used they refer to the Fanning friction factor.

4.2.1. Smooth Channel. The smooth walled test section designated sfc000 was tested to compare the experimental results against reference values in the literature. The length averaged friction factor ($C_{f,m}$) for test section sfc000 is shown plotted against Reynolds number in Figure 4.2. Also shown in Figure 4.2 are friction factor versus Reynolds number correlations found in the references. The correlation labeled '4-1 Laminar' was found in [26] for laminar flow ($\mathrm{Re} < 2800$) in a rectangular

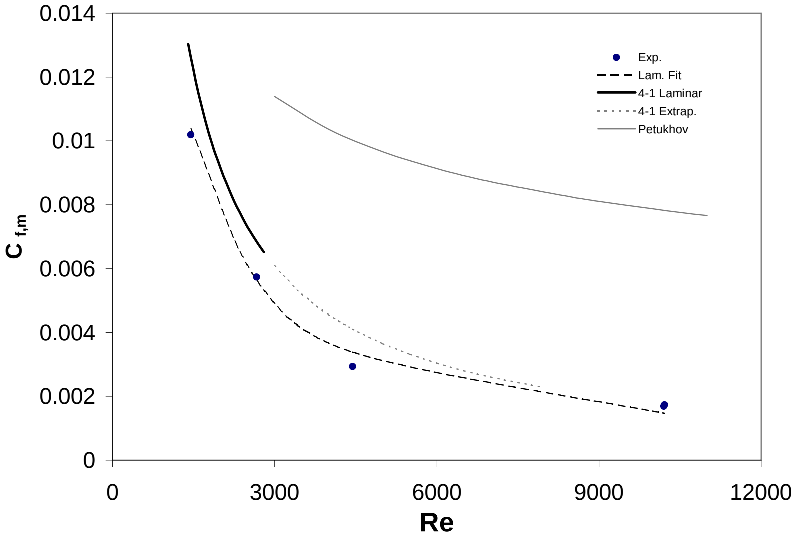

Figure 4.2: Length averaged friction factor for sfc000 compared to correlations

duct with a 4-1 aspect ratio. The formula for this curve is given in Eq. (32).

$$C_{f,m} = \frac{18.25}{\mathrm{Re}} \tag{32}$$

The actual aspect ratio of sfc000 was 3.75-1 which would cause a small expected difference between the experimental results and the reference. The '4-1 Laminar' correlation was extrapolated into the transitional range of Re as shown by the dashed line in the figure. The line labeled 'Petukhov' was also found in [26] and was a correlation for turbulent flow. The Petukhov formula is given in Eq. (33).

$$C_{f,m} = 1/4\left(0.790\ln\mathrm{Re} - 1.64\right)^{-2} \tag{33}$$

All experimental points in Figure 4.2 up to Re $\approx$ 4500 are in good agreement with the '4-1 Laminar' correlation with the experimental points being slightly below the reference. A curve was fit to the experimental points in the laminar flow region with the resulting equation shown as Eq. (34).

$$C_{f,m}\mathrm{Re} = 15.04 \tag{34}$$

The relationship found in Eq. (34) was extended to Re $\approx$ 10000 for comparison with the experimental data as shown by the 'Lam. Fit' line in Figure 4.2. It would be expected for the flow to begin transitioning from laminar to turbulent flow around Re = 2800 for a channel with a rectangular cross-section according to information in [26]. However, the experimental data points at Re $\approx$ 4500 and Re $\approx$ 10000 appear to follow the laminar relationship between $C_{f,m}$ and Re much more closely than the turbulent 'Petukhov' line. An explanation for laminar behavior in what would normally be considered the turbulent range of Reynolds numbers was given by Schlichting [27]. It was reported that if the inlet flow was made free from disturbances laminar flow could be maintained for Reynolds numbers as high as 40,000. The flow visualization tests performed on the current experimental setup showed that the flow entering test section sfc000 was very uniform with only minor disturbances even at high Reynolds numbers. So, it was not too suprising that the flow exhibited laminar rather than turbulent characteristics.

4.2.2. Bumped Wall Channels. A plot comparing the length averaged friction factor versus Reynolds number for all the bumped wall geometries is shown as Figure 4.3. It is interesting to note that the friction factor for sfc010 and sfc011 is nearly identical at all Reynolds numbers. The bumped wall geometry on both test sections had the same geometric dimensions but sfc011 had intermittent bumps while sfc010 had bumps along its entire length. It was expected that sfc011 would have a lower $C_{f,m}$ than sfc010 due to it having fewer bumps. One possible explanation for sfc010 and sfc011 having nearly the same $C_{f,m}$ at all Re is that the bumps on sfc011

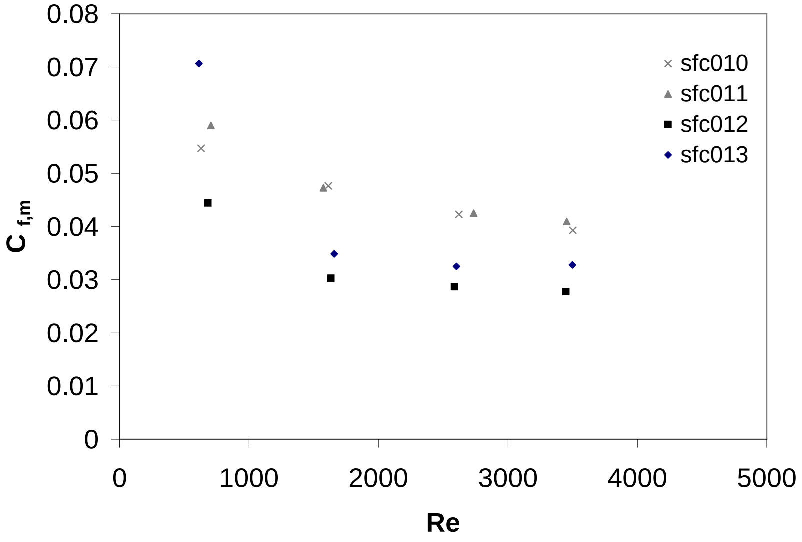

Figure 4.3: Length averaged friction factor for bumped wall geometries

extended across the entire width of the wall while the bumps on sfc010 extended across only 75% of the width.

A major change in the friction factor for sfc013 was noticed when Reynolds number increased from 600 to 1600. For all the other bumped geometries there was a drop in friction factor over this range of Reynolds numbers, but the drop was not nearly as large as for sfc013. A key difference between sfc013 and the other three bumped geometries was that the ratio of bump pitch-to-channel width (L_1/H_s) was equal to 2.0 while for the other three geometries the ratio was 3.0. A comparison was made to information found by Comini et al. [28] which studied transition in a corrugated channel. In [28] it was found that for $\beta = 30°$ and $L_1/H_s = 2.22$ a higher Reynolds number was required for transitional flow than when $L_1/H_s = 2.86$. Thus, it would be expected for sfc013 to transition from laminar flow to turbulent flow at a higher Reynolds number than the other geometries. The general trend in $C_{f,m}$ during transition for a circular tube is shown in Figure 4.4. The curve for the transitional

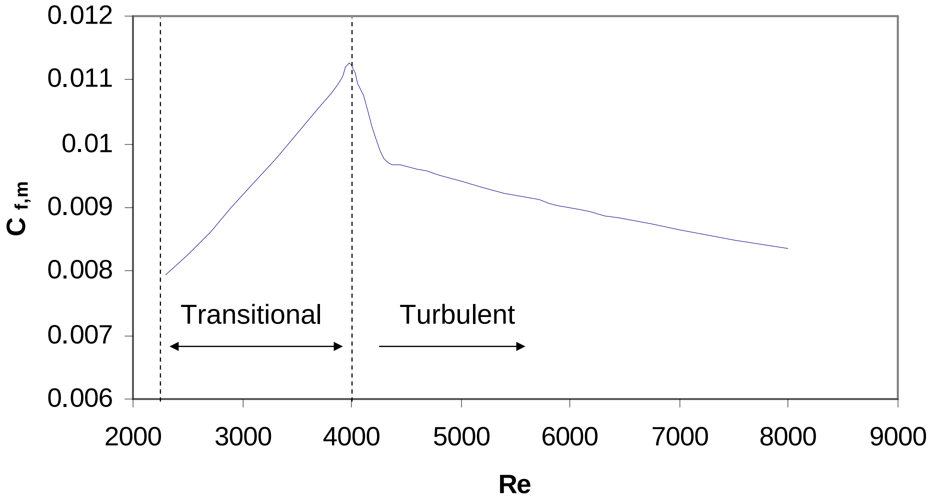

Figure 4.4: Friction factor during transition to turbulent flow

$C_{f,m}$ was found in [29] and the formula for the curve is shown in Eq. (35).

$$C_{f,m} = 2.3\text{x}10^{-8}\text{Re}^{3/2} + 0.0054 \tag{35}$$

For turbulent flow, the Petukhov relation given in Eq. (33) was again used. From Figure 4.4 it can be seen that during transition $C_{f,m}$ increases as Reynolds number increases, but once the flow becomes turbulent $C_{f,m}$ begins to fall. Combining the information from [28] and the trends noted from Figure 4.4 it is believed that at Re = 600 the flow through sfc013 had not yet fully transitioned to turbulent flow. However, it appears that all the other bumped walled channels had turbulent flow at Re = 600. Thus, if a lower $C_{f,m}$ is desired at Re = 600, then $L_1/H_s = 3.0$ is a better choice since the flow will have already transitioned to the turbulent regime.

The ratio of the bump height-to-hydraulic diameter (H_2/D_h) was another parameter that varied on the bumped walled test sections. Sections sfc010 and sfc011 had a ratio of 0.177 while sections sfc012 and sfc013 had a ratio of 0.127. It was expected that a smaller value for H_2/D_h would result in a lower $C_{f,m}$ since the bumps would be shorter and cause less of a flow disruption. This result was confirmed by noting that in Figure 4.3 the points for sfc012 and sfc013 are below the points for sfc010 and sfc011 once Re $\geq$ 1600. The bump pitch-to-bump height ratio (L_1/H_2) also varied among the test sections. Three different values for this ratio were used. The values of L_1/H_2 for test sections sfc010, sfc011, sfc012, and sfc013 were 10.7, 10.7, 15, and 10 respectively. A plot of $C_{f,m}$ against L_1/H_2 at Re = 2600 is shown in Figure 4.5. As shown in Figure 4.5, for Re $\geq$ 1600 the general trend is for $C_{f,m}$ to decrease as L_1/H_2 increases. A table summarizing all the important geometric ratios is shown in Table 4.3.

Several different fin types with geometric ratios similar to those used in the bumped wall test sections were selected from [30] for comparison to the bumped fin geometries. A plot comparing the four bumped wall geometries to the geometries from [30] is shown as Figure 4.6. In Figure 4.6, the curve labeled '9.03' was a plain fin surface without any bumps or other enhancement, the curve '3/8(b)-11.1' was a louvered fin, '3/32-12.22' was an offset-strip fin, and '11.5-3/8W' was a wavy fin. As expected, the bumped geometries all had a higher friction factor than the plain fin. When compared to the louvered fin, sfc010 and sfc011 had higher friction factors while sfc012 and sfc013 were lower for the majority of the Reynolds number range. The offset strip fins and the wavy fins had higher friction factors than all the bumped fins.

The variation in the friction factor along the length of the bumped wall test sections was another result of the experimental tests. The variation in friction factor was examined to determine when and if the flow became hydrodynamically fully developed. A plot of the local friction factor is shown in Figure 4.7 at four different Reynolds numbers for test section sfc010. Also in the figure are correlations for the distribution of the friction factor for developing flow in a smooth channel found in [31]. These correlations are the lines labeled 'Sm 600' and 'Sm 1600' in Figure 4.7. For a smooth channel with laminar flow, the flow is expected to be hydrodynamically

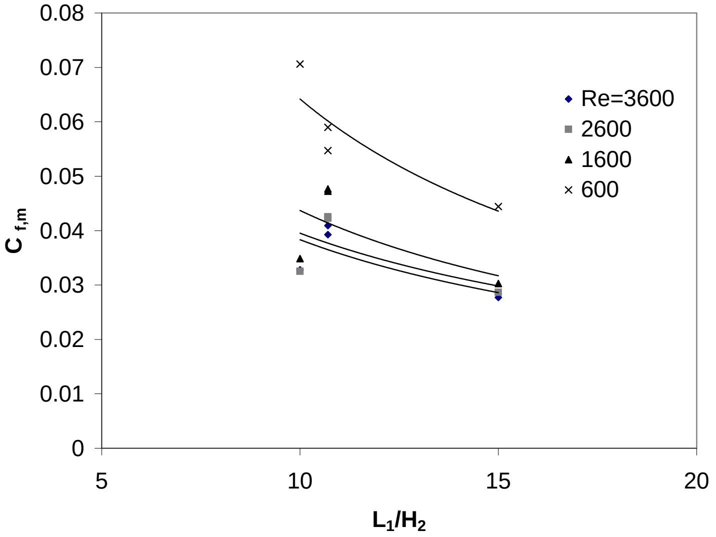

Figure 4.5: Friction factor for different bump pitch-to-height ratios over range of Re

Table 4.3: Geometric ratios for test sections

Test Section	L_1/H_s	H_2/D_h	L_1/H_2
sfc010	3.0	0.177	10.7
sfc011	3.0	0.177	10.7
sfc012	3.0	0.127	15
sfc013	2.0	0.127	10

fully developed once $x^+ > 0.056$ according to Shah and London [31]. The flow has fully developed if the friction factor becomes constant and is no longer a function of position. As seen in the figure, for Re=1600, 2600, and 3600 the friction factor is nearly constant even for values of x^+ below 0.01. Only at Re=600 does the friction factor drop appreciably and not reach a constant value by the outlet of the test section. From these observations, it is concluded that the flow was hydrodynamically fully developed well before the outlet of the test section for Re $\geq$ 1600. The reason for the flow developing in a much shorter length than for a smooth channel is likely due

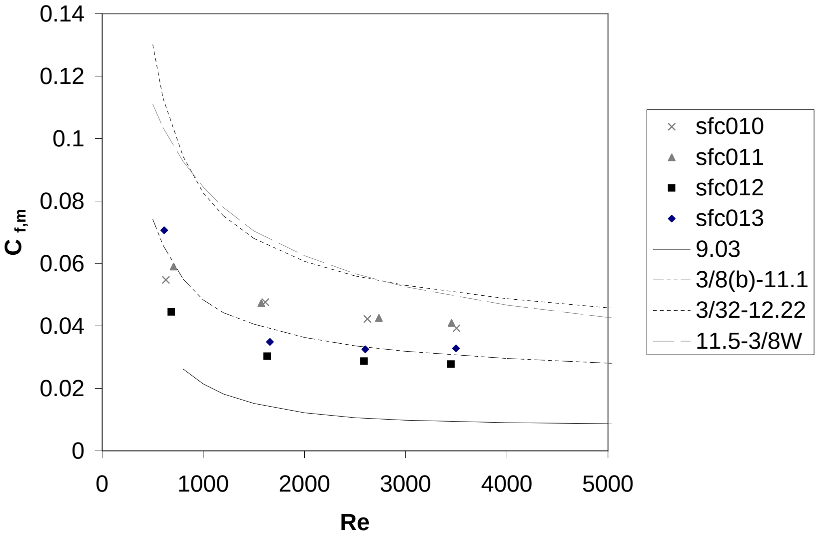

Figure 4.6: Friction factor of bumped geometries compared to geometries from literature

to the fact that the flow had transitioned toward turbulent flow for these Reynolds numbers. Turbulent flow becomes hydrodynamically fully developed in a much shorter flow length than laminar flow with the difference typically being an order of magnitude according to Kays et al. [32].

It was desired to determine if the same hydrodynamic development trends were found for the other bumped wall geometries. Similar results to those found for sfc010 were found for sfc012 and sfc013. Both geometries showed very little change in friction factor over the length of the test section when Re $\geq$ 1600. However, for sfc011 the friction factor was found to increase along the length of the test section. This result can explained by noting that sfc011 had intermittent bumps along its length. The flow likely began to transition in the bumped regions but then tended back toward laminar flow in the flat walled regions. As was noted earlier from Figure 4.4, when the flow just begins to transition the friction factor increases. For test section sfc011 this likely means that the flow never completely transitioned to turbulent flow because if it had, a decrease in friction factor should have been found.

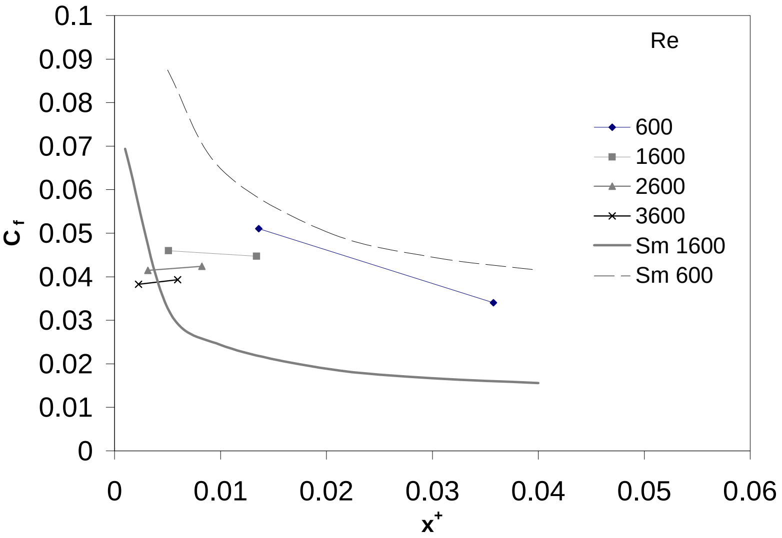

Figure 4.7: Local friction factor at various Re for section sfc010

4.3. HEAT TRANSFER RESULTS

The results of the experimental tests allowed the heat transfer coefficient to be found along the length of the test sections as described in Section 4.1.6. The heat transfer characteristics of each test section are presented in nondimensional form using Nusselt number, Stanton number, and Colburn j factor in the following sections. A calculation showed the uncertainty in the heat transfer results to be 9% or less for all reported values.

4.3.1. Smooth Channel. A plot of the length averaged Nusselt number (Nu_m) for the smooth walled test section sfc000 is shown in Figure 4.8. Along with the experimental data several correlations from the literature for thermally fully developed flow are shown in Figure 4.8. The curve labeled ‘Gnielinski’ was from [26] for turbulent flow. The corresponding Gnielinski equation is shown in Eq. (36).

$$\mathrm{Nu}_m = \frac{(C_f/2)\,(\mathrm{Re}-1000)\,\mathrm{Pr}}{1+12.7\,(C_f/2)^{1/2}\left(\mathrm{Pr}^{2/3}-1\right)} \tag{36}$$

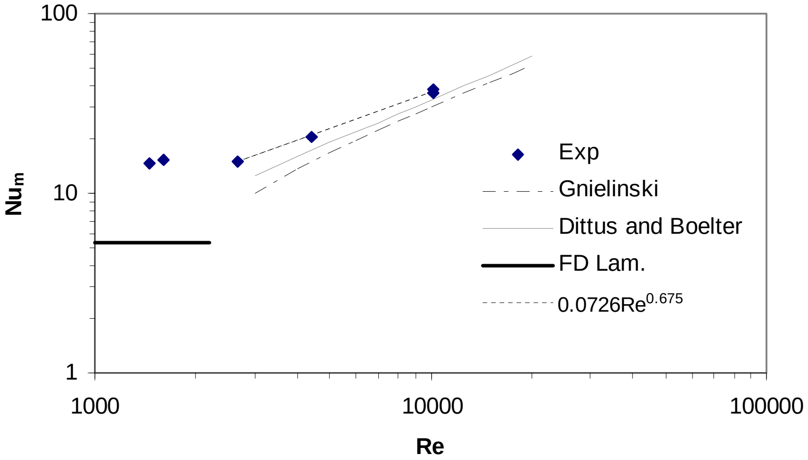

Figure 4.8: Length averaged Nusselt number for test section sfc000

The value used for C_f in Eq. (36) was found using the Petukhov relationship given earlier in Eq. (33). The Dittus Boelter equation is also shown in the figure. The equation for the Dittus Boelter relationship is given in Eq. (37) as found in [32].

$$\mathrm{Nu}_m = 0.024\mathrm{Re}^{0.8}\mathrm{Pr}^{0.4} \tag{37}$$

Also shown in Figure 4.8 is the Nusselt number curve for thermally fully developed laminar flow in a rectangular duct with a 4-1 aspect ratio. This curve is labeled 'FD Lam' and shows that for laminar flow the Nusselt number is expected to be constant at 5.3.

From Figure 4.8, it is seen that the experimental Nu_m is nearly constant at 15.0 for $\mathrm{Re} < 2500$. This observation leads to the conclusion that the flow was likely laminar through this range of Re. The experimental Nu_m value was larger than the laminar fully developed value since the flow in the test section was not fully developed. The test section length was equal to about 30 hydraulic diameters ($L/D_h = 30$) and laminar flow at $\mathrm{Re} = 1500$ is not be expected to fully develop thermally until after 145 hydraulic diameters according to Shah and London [31]. For undeveloped flow the Nusselt number is always larger than the fully developed value due to the very thin boundary layer near the inlet of the channel.

For $\mathrm{Re} > 2500$ the experimental value for Nu_m increased as Re increased. This increase was in good agreement with the turbulent correlations indicating that the flow became turbulent in this range of Re. A curve was fit to the experimental data points for $\mathrm{Re} > 2500$ and its equation is given in Eq. (38).

$$\mathrm{Nu}_m = 0.0726\mathrm{Re}^{0.675} \tag{38}$$

The difference between the experimental values and the correlations was much smaller in the turbulent range. The reason for the smaller difference is that turbulent flow develops over a much shorter distance. Since the correlations were for fully developed turbulent flow, the sooner the experimental flow developed the better the experimental results would match the correlations. An equation found in [32] gave the ratio of the length averaged Nusselt number to the fully developed Nusselt number (Nu_∞) for turbulent developing flow as shown in Eq. (39).

$$\frac{\mathrm{Nu}_m}{\mathrm{Nu}_\infty} = 1 + \frac{C}{x/D_h} \tag{39}$$

For a sudden contraction entrance, the value for C was 6.0. Evaluating Eq. (39) at $x/D_h = 30$, the Nusselt number was expected to be enhanced 20% over the fully developed value. Comparing the experimental data point at $\mathrm{Re} = 4500$ to the Gnielinski correlation found that the experimental average Nusselt number was enhanced 17.7% which was in good agreement with the predicted value.

4.3.2. Bumped Wall Channels. The heat transfer characteristics of the bumped wall test sections are shown in Figure 4.9 where the length averaged Colburn j factor has been plotted against Reynolds number. From Figure 4.9 it can be seen that for $\mathrm{Re} \geq 1600$ the j_m values for sfc011, sfc012, and sfc013 are all nearly identical.

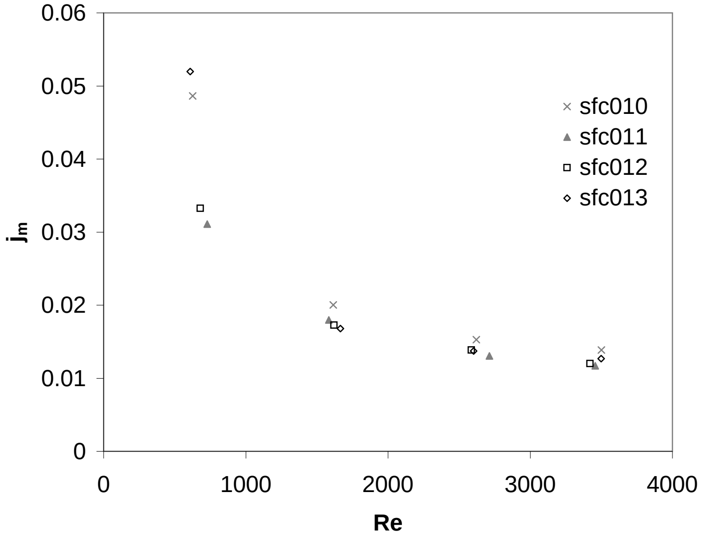

Figure 4.9: Colburn j_m factor for bumped wall geometries

The j_m values for sfc010 are only slightly above those for the other three bumped wall sections in this Re range. At Re = 600, sfc010 and sfc013 have a much higher value for j_m than sfc011 and sfc013. The behavior of sfc013 and sfc010 at Re = 600 can be explained by examining Figure 4.10 which shows length averaged Nusselt number plotted against Reynolds number. From the figure, it is seen that when Re increases from 600 to 1600 the value of Nu$_m$ remains nearly constant for sfc010 while for sfc013 the Nu$_m$ value actually drops. A constant Nu$_m$ over a range of Re is an indication of laminar flow so it appears that sfc010 may still be laminar. Test section sfc013, though, exhibits strange behavior that is not typical for laminar or turbulent flow. However, as noted earlier sfc013 was the only test section with $L_1/H_s = 2.0$ while the others had $L_1/H_s = 3.0$. Comini et al. [28] found that a corrugated duct with $L_1/H_s = 2.86$ transitioned at a lower Re and had greater enhancement of Nu$_m$ than a duct with $L_1/H_s = 2.22$. This trend appears to hold for sfc011 and sfc012 when compared to sfc013, but it is harder to say the same about sfc010 in comparison to sfc013. Further tests may need to be conducted to verify the behavior of sfc013 at low Reynolds numbers.

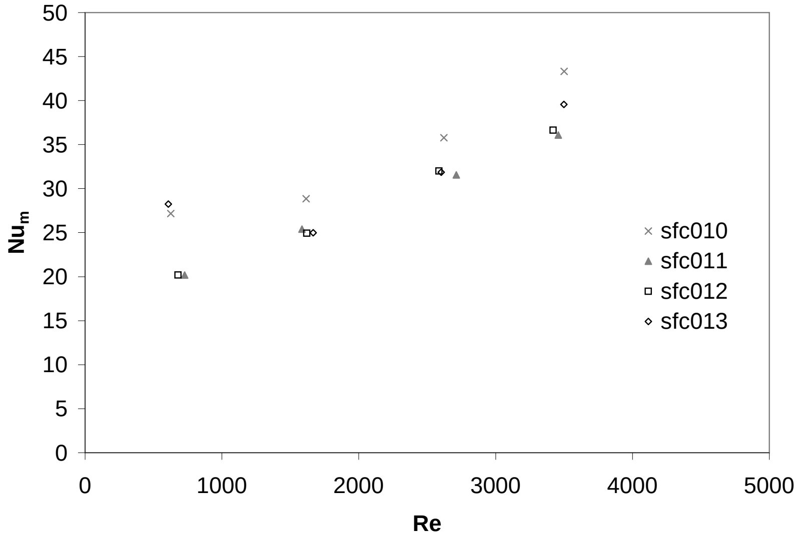

Figure 4.10: Length averaged Nusselt number for bumped wall geometries

A plot comparing the values of j_m for the bumped wall test sections to the same geometries selected earlier from [30] for the friction factor comparison is shown in Figure 4.11. All the experimentally tested bumped wall geometries had j_m values above those for the geometries from [30]. An explanation for finding larger values could be that Kays and London [30] tested an entire heat exchanger core with upstream and downstream ducts. The upstream duct would have allowed a hydrodynamic boundary layer to form on the walls. The boundary layer would have caused the velocity profile across the face of the tested heat exchanger to not be uniform. Near the walls the air velocity would have been lower than in the center of the duct. Since the results in [30] were average values for the entire exchanger core, the lower heat transfer coefficients in the channels near the outside of the core would have depressed the overall values.

4.4. COMPARISON OF HEAT TRANSFER SURFACES

All of the heat transfer surfaces experimentally studied were compared to one another using two different measures. The first was the flow area goodness factor (ε_a)

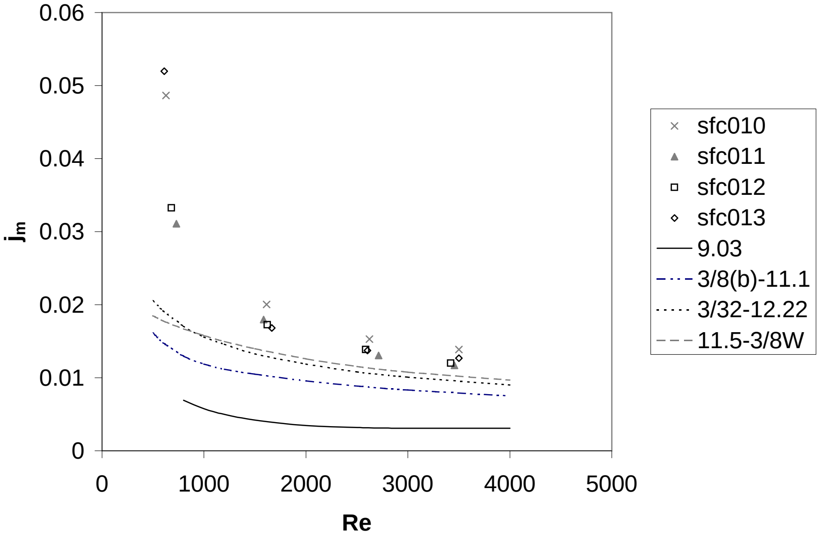

Figure 4.11: Colburn j_m factor for bumped walls compared to reference geometries

and the second was the volume goodness factor. The flow area goodness factor was found in [33] and is defined as shown in Eq. (40).

$$\varepsilon_a = \frac{j}{C_f} \tag{40}$$

A higher value for ε_a indicates the surface requires a lower free flow area and also a lower frontal area to transfer a given amount of heat. This is an important measure as it is often desirable to make the frontal area of a heat exchanger as small as possible. However, sometimes using a surface that requires a small frontal area leads to the need for a longer flow length through the exchanger and hence a larger volume. This brings to light the need for a comparison measure that accounts for the volume required by a heat transfer surface when used in a heat exchanger. Fortunately, the volume goodness factor fills this need.

The volume goodness factor is defined in [31] but cannot be represented by a single number in the same way as area goodness factor. The volume goodness factor for a surface is found by plotting h_{std} versus E_{std}. The definitions for h_{std} and E_{std} were given in [31] and are shown below as Eq. (41) and Eq. (42).

$$h_{std} = \frac{C_p \mu}{\mathrm{Pr}^{2/3}} \frac{1}{D_h} j \mathrm{Re} \tag{41}$$

$$E_{std} = \frac{1}{2} \frac{\mu^3}{\rho^2} \frac{1}{D_h^3} C_f \mathrm{Re}^3 \tag{42}$$

The physical quantity represented by h_{std} is the heat transfer power per unit temperature difference per unit surface area while E_{std} represents the friction power per unit of surface area. The *std* subscripts in h_{std} and E_{std} show that the fluid properties should all be evaluated at a standard temperature and pressure that is appropriate for the intended application of the heat exchanger and assumed to be constant. A higher position on a h_{std} versus E_{std} plot means the heat transfer surface transfers more heat for a given volume and thus would require a smaller overall heat exchanger volume to transfer a given amount of heat.

According to Shah [33], oftentimes when surfaces are compared based on area goodness factors and volume goodness factors the surface with the best area goodness factor will not have the best volume goodness factor and vice versa. It is then necessary to determine what balance is acceptable between frontal area and overall volume.

4.4.1. Flow Area Goodness Factor. The flow area goodness factor for all the bumped wall geometries was calculated and a plot of ε_a against Reynolds number is shown in Figure 4.12. From Figure 4.12 it can be seen that sfc012 has the highest ε_a at all Reynolds numbers except Re = 600. At Re = 600 only sfc010 has a higher ε_a than sfc012.

4.4.2. Volume Goodness Factor. To create the plot to find the volume goodness factor for the bumped wall geometries, a standard temperature and pressure had to first be selected. The selected conditions were in the middle of the range specified by ATS. The selected temperature was 50°C and the selected pressure was 1 atm. The working fluid was assumed to be dry air and when the required properties were evaluated the values shown in Table 4.4 were found. The plot for determining the volume goodness factor of the bumped wall geometries is shown as Figure 4.13. Looking at Figure 4.13, it is found that sfc010 has the highest curve and hence the highest volume goodness factor over the range of the graph except for at the smallest values of E_{std}. Another interesting observation from the figure is that sfc012 (which had the highest ε_a) consistently has a lower volume goodness factor than sfc010 although the difference gets smaller as E_{std} increases. Thus, as predicted by Shah [33], this performance comparison finds that the surface with the best ε_a is not the same surface that has the highest volume goodness factor.

4.4.3. Bumped Wall Geometry Comparison. Since sfc012 and sfc010 were the best geometries based on flow area goodness and volume goodness, respectively, a calculation was performed to quantify the difference in required heat exchanger size. A Reynolds number of 2000 was used in the flow area comparison. A curve was fit to the data shown in Figure 4.12 for both sfc010 and sfc012. The resulting curve fit for sfc010 is shown in Eq. (43).

$$\varepsilon_a = 6.7589\mathrm{Re}^{-0.3364} \tag{43}$$

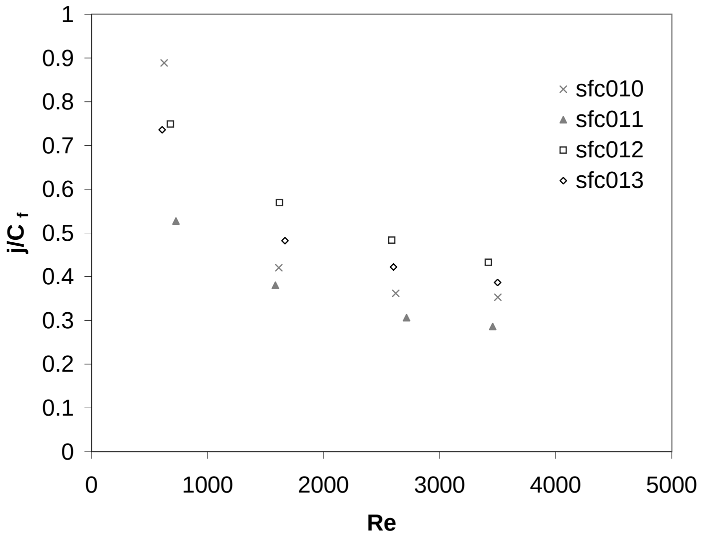

Figure 4.12: Flow area goodness factor for bumped wall geometries

Table 4.4: Air properties for volume goodness factor comparison

C_p ($\frac{\text{J}}{\text{kgK}}$)	μ ($\frac{\text{kg}}{\text{ms}}$)	ρ ($\frac{\text{kg}}{\text{m}^3}$)
1006	19.29x10^{-6}	1.106
Dry air at $T = 50$°C and 1 atm		

For sfc012 the curve fit is shown in Eq. (44).

$$\varepsilon_a = 29.752\text{Re}^{-0.5564} \qquad (44)$$

At Re = 2000 the ε_a for sfc010 was found to be 0.433 and for sfc012 ε_a was found to be 0.524. Since ε_a is inversely proportional to the flow area squared ($\varepsilon_a \propto \frac{1}{A^2}$), sfc012 would require a 9% smaller frontal area than sfc010 at this Re. To compare the exchanger volume required for sfc010 and sfc012, E_{std} was assumed to be equal for both surfaces at a value of 0.03 W/m^2. It is found from Figure 4.13 that $h_{std} =$

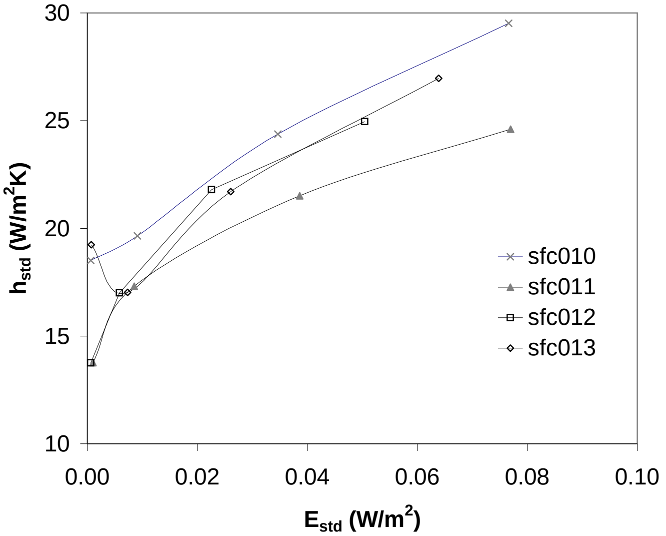

Figure 4.13: Plot for determining volume goodness factor of bumped wall geometries

23.46 $\frac{\mathrm{W}}{\mathrm{m^2K}}$ for sfc010 and $h_{std} = 22.5\ \frac{\mathrm{W}}{\mathrm{m^2K}}$ for sfc012. Thus, sfc010 would require 4% less overall heat transfer area than sfc012 for this value of E_{std}, resulting in a smaller overall exchanger volume.

Looking at ratios of geometric parameters for the bumped wall surfaces gives some insight in to what values should be used for a given objective. In terms of the flow area goodness factor, for a constant value of $L_1/H_s = 3.0$ a 23-35% higher ε_a value can be obtained by decreasing H_2/D_h from 0.177 to 0.127. When $H_2/D_h = 0.127$ is held constant but L_1/H_s decreases from 3.0 to 2.0, there is also a decrease in ε_a between 10-15%. The volume goodness factor also shows some trends depending on the selected geometric ratios. Holding $L_1/H_s = 3.0$ constant and decreasing H_2/D_h from 0.177 to 0.127 results in a decrease in volume goodness factor between 2.3-8.4%. Changing L_1/H_s from 3.0 to 2.0 while holding $H_2/D_h = 0.127$ constant results in a very small change in volume goodness factor with the largest difference being less than 2%.

5. SUMMARY AND RECOMMENDATIONS

5.1. SUMMARY OF RESULTS

This thesis has focused on the experimental testing of enhanced air fins. The development of an experimental testing program to determine the heat transfer and friction characteristics was discussed. The results from the experimental tests can be summarized by the following.

- Tests were performed using air as the working fluid over a range of Reynolds numbers from 600 to 3600. Pressure drop and temperature were measured along the length of the test section to find the friction and heat transfer characteristics of each test section.

- Smooth walled test sections were used to validate the measurement techniques and the experimental setup. Results of the smooth walled tests were in good agreement with results from the literature.

- Test sections with enhanced surfaces had rectangular cross-sections with a 3.75-to-1.0 aspect ratio. The narrower top and bottom walls of the tests section were smooth, while the side walls had the bumped geometry machined into them.

- A comparison was made for the Fanning friction factor and the Colburn j factor results to results for similar geometries in the literature. Good agreement was found for the current geometries.

- Transition from laminar flow to turbulent flow appeared to occur between $\mathrm{Re} = 600$ and $\mathrm{Re} = 1600$ for the bumped wall geometries.

- The bumped wall geometries were compared to one another using the flow area goodness factor and the volume goodness factor. Geometry sfc012 had the highest flow area goodness factor, while geometry sfc010 had the best volume goodness factor.

- The highest flow area goodness factor for the tested geometries was found for the L_1/H_s value of 3.0 and the H_2/D_h value of 0.127. A greater increase in area goodness factor was found when L_1/H_s increased from 2.0 to 3.0 than when H_2/D_h changed from 0.177 to 0.127. The change in L_1/H_s caused a 23-35% increase in area goodness factor, while the change in H_2/D_h only caused a 10-15% increase.

- For the best volume goodness factor, the H_2/D_h value should be 0.177. The dependence of volume goodness factor on L_1/H_s was minimal and a value of either $L_1/H_s = 2.0$ or $L_1/H_s = 3.0$ gave nearly the same volume goodness factor.

- The intermittent bumped wall geometry on test section sfc011 did not appear very promising in comparison to the continuously bumped walls from the perspective of flow area goodness factor or volume goodness factor. A difference in the machined wall geometry may have caused this result and intermittent bumps should not be discounted in the future.

5.2. RECOMMENDATIONS FOR FUTURE WORK

Many of the experimental results showed a different trend in the Reynolds number range from 600 to 1600 than when Reynolds number was greater than 1600. Further tests are recommended in the $600 < \mathrm{Re} < 1600$ range to refine the results. The largest experimental uncertainties were present for the points at $\mathrm{Re} = 600$, so the uncertainty may have contributed to the different behavior. The uncertainty at lower Reynolds numbers could be mitigated by using test sections scaled from the production scale by a smaller factor than was used in the current experiments. Then, the measured differential pressures, output powers from the heaters, and differential temperatures (which were the largest contributors to the overall uncertainty) would be larger and not contribute as much uncertainty to the overall results.

Another recommendation would be to machine a test section with the same intermittent bump pattern as sfc011 but with the bump only covering the same portion of the wall as on the other test sections. The walls on sfc011 were bumped across their full width while the other test sections were only bumped across 75% of their width. Full width bumps were easier to machine, but geometric similitude was lost.

Lastly, more values of the L_1/H_s and H_2/D_h ratios should be tested. Values of L_1/H_s above 3.0 may give an even better flow area goodness factor without adversely affecting the volume goodness factor. Values of H_2/D_h below 0.127 should also be studied since a large increase in area goodness factor was found when H_2/D_h changed from 0.177 to 0.127. However, when H_2/D_h becomes too small, the gain in area goodness factor is expected to be greatly offset by a marked decrease in volume goodness factor.

BIBLIOGRAPHY

[1] J. Nikuradse. Laws of flow in rough pipes. Technical Report TM 1292, NACA, 1933.

[2] R.L. Webb, E.R.G. Eckert, and R.J. Goldstein. Heat transfer and friction in tubes with repeated-rib roughness. *Int. J. Heat Mass Transfer*, 14:601–616, 1971.

[3] J.C. Han, L.R. Glicksman, and W.M. Rohsenow. An investigation of heat transfer and friction for rib-roughened surfaces. *Int. J. Heat Mass Transfer*, 21:1143–1156, 1978.

[4] J.C. Han. Heat transfer and friction in channels with two opposite rib-roughened walls. *ASME J. Heat Transfer*, 106:774–781, 1984.

[5] J.C. Han. Heat transfer and friction characteristics in rectangular channels with rib turbulators. *ASME J. Heat Transfer*, 110:321–328, 1988.

[6] J.C. Han, S. Ou, J.S. Park, and C.K Lei. Augmented heat transfer in rectangular channels of narrow aspect ratios with rib turbulators. *Int. J. Heat Mass Transfer*, 32:1619–1630, 1989.

[7] M. Greiner, R.-F. Chen, and R.A. Wirtz. Augmented heat transfer in a recovery passage downstream from a grooved section: An example of uncoupled heat/momentum transport. *ASME J. Heat Transfer*, 117:303–308, 1995.

[8] M. Greiner, P.F. Fischer, and H.M. Tufo. Two-dimensional simulations of enhanced heat transfer in an intermittently grooved channel. *ASME J. Heat Transfer*, 124:538–545, 2002.

[9] A.M. Jacobi and R.K. Shah. Heat transfer enhancement through the use of longitudinal vortices: A review of recent progress. *Experimental Thermal and Fluid Science*, 11:295–309, 1995.

[10] S.V. Garimella and P.A. Eibeck. Enhancement of single phase convective heat transfer from protruding elements using vortex generators. *Int. J. Heat Mass Transfer*, 34:2431–2433, 1991.

[11] S.V. Garimella and P.A. Eibeck. Heat transfer characteristics of an array of protruding elements in single phase forced convection. *Int. J. Heat Mass Transfer*, 12:2659–2669, 1990.

[12] St. Tiggelbeck, N.K. Mitra, and M. Fiebig. Comparison of wing-type vortex generators for heat transfer enhancement in channel flows. *ASME J. Heat Transfer*, 116:880–885, 1994.

[13] F. Dupont, C. Gabillet, and P. Bot. Experimental study of the flow in a compact heat exchanger channel with embossed-type vortex generators. *ASME J. of Fluids Eng.*, 125:701–709, 2003.

[14] H.J. Sauer, Jr., R.H. Howell, and W.J. Coad. *Principles of Heating, Ventilating, and Air Conditioning.* ASHRAE, 2001.

[15] R.W. Miller. *Flow Measurement Engineering Handbook.* McGraw Hill, 3rd edition, 1996.

[16] E.M. Laws and J.L. Livesey. Flow through screens. In *Annual Review of Fluid Mechanics*, volume 10, pages 247–266. Annual Reviews Inc., 1978.

[17] J.B. Barlow, Jr. W.H. Rae, and A. Pope. *Low-Speed Wind Tunnel Testing.* John Wiley and Sons, Inc., 3rd edition, 1999.

[18] R.P. Benedict. *Fundamentals of Temperature, Pressure, and Flow Measurements.* John Wiley and Sons, 3rd edition, 1984.

[19] *ASHRAE Standard 41.2-1987: Standard Methods for Labratory Airflow Measurements.* American Society of Heating, Refrigeration, and Air-Conditioning Engineers, 1987.

[20] R.W. Hyland and A. Wexler. Formulations for the thermodynamic properties of dry air from 173.15 K to 473.15 K and of saturated moist air from 173.15 Kto 372.15 K, at pressures to 5 MPa. *ASHRAE Transactions*, 89(2):520–531, 1983.

[21] *Thermophysical Properties of Humid Air.* M. Conde Engineering, 2005.

[22] E.A. Mason and L. Monchick. Survey of the equation of state and transport properties of moist gases. In A. Wexler, editor, *Humidity and Moisture: Measurement and Control in Science and Industry*, volume 3, pages 257–272. Reinhold Publishing Corp., 1965.

[23] F.E. Jones. The air density equation and the transfer of mass unit. Technical Report NBSIR 77-1278, National Bureau of Standards, July 1977.

[24] R.W. Hyland and A. Wexler. Formulations for the thermodynamic properties of saturated phases of H_2O from 173.15 k to 473.15 k. *ASHRAE Transactions*, 89 (2):500–511, 1983.

[25] *Temperature Measurement Handbook.* Nanmac Corp., 12th edition, 2006.

[26] A.F. Mills. *Heat Transfer.* Prentice Hall, 2nd edition, 1999.

[27] H. Schlichting. *Boundary Layer Theory.* McGraw-Hill, 4th edition, 1960.

[28] G. Comini, C. Nonino, and S. Savino. Effect of space ratio and corrugation angle on convection enhancement in wavy channels. *Int. J. Numerical Methods for Heat & Fluid Flow*, 13(4):500–519, 2003.

[29] M.S. Bhatti and R.K. Shah. *Handbook of Single-Phase Convective Heat Transfer.* John Wiley & Sons, 1987.

[30] W.M. Kays and A.L. London. *Compact Heat Exchangers.* McGraw-Hill, 3rd edition, 1984.

[31] R.K. Shah and A.L. London. Laminar flow forced convection in ducts. In *Advances in Heat Transfer.* Academic Press, 1978.

[32] W.M. Kays, M.E. Crawford, and B. Weigand. *Convective Heat and Mass Transfer.* McGraw-Hill, 4th edition, 2005.

[33] R.K. Shah. Compact heat exchanger surface selection methods. In *Sixth International Heat Transfer Conference*, volume 4, pages 193–199, 1978.

VITA

Stephen John Dale Rucker was born on December 19, 1982 in Savannah, Missouri. In May 2001, he graduated from Savannah High School. During the fall of 2001 he enrolled at the University of Missouri-Rolla (UMR) studying mechanical engineering. He graduated with his B.S. degree in Mechanical Engineering from UMR in May 2005. That summer, he began his graduate work under Dr. Kelly Homan in the mechanical engineering department at UMR. In August 2007, he graduated from UMR with his M.S. degree in Mechanical Engineering.